

The Stability and Slow Dynamics of Localized Spot Patterns for the 3-D Schnakenberg Reaction-Diffusion Model*

J. C. Tzou[†], S. Xie[‡], T. Kolokolnikov[‡], and M. J. Ward[§]

Abstract. On a bounded three-dimensional domain Ω , a hybrid asymptotic-numerical method is employed to analyze the existence, linear stability, and slow dynamics of localized quasi-equilibrium multispot patterns of the Schnakenberg activator-inhibitor model with bulk feed-rate A in the singularly perturbed limit of small diffusivity ε^2 of the activator component. By approximating each spot as a Coulomb singularity, a nonlinear system of equations is formulated for the strength of each spot. To leading order in ε , two types of solutions are identified: symmetric patterns for which all strengths are identical, and asymmetric patterns for which each strength takes on one of two distinct values. The $\mathcal{O}(\varepsilon)$ correction to the strengths is found to depend on the spatial configuration of the spots through a certain Neumann Green's matrix \mathcal{G} . When $\mathbf{e} = (1, \dots, 1)^T$ is not an eigenvector of \mathcal{G} , a detailed numerical and (in the case of two spots) asymptotic characterization is performed for the resulting imperfection-sensitive bifurcation structure. For symmetric multispot patterns, a leading-order global threshold in terms of $|\Omega|$ and parameters of the Schnakenberg model is obtained, below which a competition instability is triggered leading to the annihilation of one or more spots. A corresponding refined threshold is established in terms of eigenvalues of \mathcal{G} in the special case when $\mathcal{G}\mathbf{e} = k\mathbf{e}$. Additionally, a local self-replication threshold for the strength of each spot is derived numerically, above which a spot splits into two. By examining $\mathcal{O}(\varepsilon)$ corrections to spot strengths, a prediction is made as to which spot will be next to split as A is slowly tuned. When the pattern is stable to $\mathcal{O}(1)$ instabilities, it is shown that the locations of spots in a quasi-equilibrium configuration evolve on a long $\mathcal{O}(\varepsilon^{-3})$ time-scale according to an ODE system characterized by a gradient flow of a certain discrete energy \mathcal{H} , the minima of which define stable equilibrium points of the ODE. The theory also illustrates that new equilibrium points can be created when $A = A(\mathbf{x})$ is spatially variable, and that finite-time pinning away from minima of \mathcal{H} can occur when $A(\mathbf{x})$ is localized. The theory for linear stability and slow dynamics when Ω is the unit ball are compared favorably to numerical solutions of the Schnakenberg PDE.

Key words. reaction-diffusion system, localized spot patterns in three dimensions, stability analysis, slow dynamics

AMS subject classifications. 35K57, 35B35, 35B36, 35B40, 35C20

DOI. 10.1137/16M108121X

*Received by the editors June 23, 2016; accepted for publication (in revised form) by T. Wanner October 6, 2016; published electronically January 31, 2017.

<http://www.siam.org/journals/siads/16-1/M108121.html>

Funding: The work of the first author was partially supported by a PIMS CRG Postdoctoral Fellowship. The work of the third author was supported by Discovery grant RGPIN-33798 and Accelerator Supplement grant RGPAS/461907. The work of the fourth author was supported by NSERC Discovery grant 81541.

[†]Corresponding author. Department of Mathematics, University of British Columbia, Vancouver, BC V6T 1Z4, Canada (tzou.justin@gmail.com).

[‡]Department of Mathematics and Statistics, Dalhousie University, Halifax, NS B3H 4R2, Canada (xieshuanguan2013@gmail.com, tkolokol@gmail.com).

[§]Department of Mathematics, University of British Columbia, Vancouver, BC V6T 1Z4, Canada (ward@math.ubc.ca).

1. Introduction. Localized spatio-temporal patterns, consisting of a collection of spots, have been observed in many diverse physical and chemical experiments (see the survey [19]). Such localized far-from-equilibrium patterns (cf. [13]) can exhibit a wide variety of dynamical phenomena including spot self-replication, spot annihilation, spot amplitude temporal oscillations, and slow spot drift. From a mathematical viewpoint, a spot pattern for a reaction-diffusion (RD) system in a multidimensional domain Ω is a spatial pattern where at least one of the solution components is highly localized near certain discrete points in the domain that can evolve dynamically in time. In two-dimensional (2-D) spatial domains there are now many studies of the stability and dynamics of localized spot patterns for certain well-known RD systems such as the Gierer–Meinhardt model (cf. [22]), the Gray–Scott model (cf. [24], [23], [2]), the Schnakenberg model (cf. [12], [25], [26]), and the Brusselator model (cf. [14], [18]). A more complete list of references on applications of, and results for, 2-D spot patterns, and corresponding one-dimensional spike patterns, in the context of RD modeling is given in the references of these cited papers.

The new focus of this paper is to provide the first systematic asymptotic study of the stability and dynamics of spot patterns in an arbitrary bounded three-dimensional (3-D) domain for a two-component singularly perturbed RD system. In this 3-D context, only the limiting shadow problem, derived from the large inhibitor diffusivity limit, has been analyzed previously (cf. [21], [9]). For concreteness, we will consider the Schnakenberg RD model, introduced in [15], as a particular case of an activator-substrate system, formulated originally as a simplified model of a trimolecular autocatalytic reaction with diffusion. The main value of this prototypical RD model has been for studying various new aspects of pattern formation in RD systems such as the effect of domain growth (cf. [1], [4]), the effect of time-delay in the reaction-kinetics (cf. [7]), the existence and stability of spikes in one dimension (cf. [10], [20]), self-replicating and slow-drifting spot phenomena in two dimensions [12], and, more recently, rotational spot dynamics in [26].

In dimensionless form, the Schnakenberg RD model (cf. [15]) is

$$(1.1a) \quad \mathcal{V}_t = \varepsilon^2 \Delta \mathcal{V} + b - \mathcal{V} + \mathcal{U}\mathcal{V}^2, \quad \mathbf{x} \in \Omega; \quad \partial_n \mathcal{V} = 0, \quad \mathbf{x} \in \partial\Omega,$$

$$(1.1b) \quad \mathcal{U}_t = \mathcal{D}\Delta \mathcal{U} + A - \mathcal{U}\mathcal{V}^2, \quad \mathbf{x} \in \Omega, \quad \partial_n \mathcal{U} = 0, \quad \mathbf{x} \in \partial\Omega.$$

Here, \mathcal{V} and \mathcal{U} are concentrations of the activator and inhibitor components, respectively, $\Omega \subset \mathbb{R}^3$ is a bounded 3-D domain, b and A are constant bulk activator and inhibitor feed-rates, $\mathcal{D} > 0$, and $0 < \varepsilon \ll 1$. We will show that (1.1) has localized spot solutions in the regime where $\mathcal{D} = \mathcal{O}(\varepsilon^{-4})$. To ensure that the amplitude of a spot is $\mathcal{O}(1)$ as $\varepsilon \rightarrow 0$, we introduce the rescaling $\mathcal{U} = \varepsilon^3 u$, $\mathcal{V} = \varepsilon^{-3} v$, and $\mathcal{D} = \varepsilon^{-4} D$. Discarding the negligible $\varepsilon^3 b$ term in (1.1a), we obtain the rescaled singularly perturbed Schnakenberg model

$$(1.2a) \quad v_t = \varepsilon^2 \Delta v - v + uv^2, \quad \mathbf{x} \in \Omega; \quad \partial_n v = 0, \quad \mathbf{x} \in \partial\Omega,$$

$$(1.2b) \quad \varepsilon^3 u_t = \frac{D}{\varepsilon} \Delta u + A - \frac{uv^2}{\varepsilon^3}, \quad \mathbf{x} \in \Omega; \quad \partial_n u = 0, \quad \mathbf{x} \in \partial\Omega.$$

The goal of this paper is to develop a hybrid asymptotic-numerical approach to analyze the existence, linear stability, and slow dynamics of quasi-equilibrium N -spot patterns for the 3-D RD model (1.2) in the limit $\varepsilon \rightarrow 0$. By using a formal asymptotic analysis, in section 2 an

N -spot quasi-equilibrium pattern is constructed for (1.2) when $A > 0$ is constant by asymptotically matching a local approximation of the solution near each spot to a global representation of the solution defined in terms of the Neumann Green's function of the Laplacian. The local problem near each spot, referred to as the core problem, is a simple radially symmetric BVP system that must be solved numerically. In the global, or outer, representation of the solution, each spot at a given instant in time is asymptotically approximated by a 3-D Coulomb singularity for u of strength S_j at location $\mathbf{x}_j \in \Omega$ for $j = 1, \dots, N$. We show that to within $\mathcal{O}(\varepsilon)$ terms, there are "symmetric" spot quasi-equilibria for which the source strengths S_j are given by $S_j = S_c + \mathcal{O}(\varepsilon)$ for $j = 1, \dots, N$, where the common value $S_c \equiv A|\Omega|/(4\pi N\sqrt{D})$ is independent of the spatial configuration of the spots in the domain. The $\mathcal{O}(\varepsilon)$ correction terms to the source strengths do, however, depend on the spot locations through a Neumann Green's matrix \mathcal{G} . In contrast, for the 2-D quasi-equilibrium spot patterns constructed in [12], [2], [14], and [18], it was found that the $\mathcal{O}(\varepsilon)$ deviation in a common value for the source strengths is replaced by a much larger $\mathcal{O}(\nu)$ correction, where $\nu \equiv -1/\log \varepsilon$. As a result, unless ε is extremely small, in a 2-D domain the source strengths for localized spot patterns are rather strongly coupled and do depend significantly on the overall spatial configuration of the spots.

In section 2.1 we show that, to leading order in ε , there are also branches of "asymmetric" N -spot quasi-equilibria for which the source strengths have two distinctly different values. To leading order in ε , these asymmetric quasi-equilibria all bifurcate from the symmetric solution branch at a common bifurcation point $S = S_{cf} \approx 4.52$. Upon including the $\mathcal{O}(\varepsilon)$ terms, we find that this common bifurcation point structure for the asymmetric quasi-equilibria persists only for spot configurations $\{\mathbf{x}_1, \dots, \mathbf{x}_N\}$ for which $\mathbf{e} = (1, \dots, 1)^T$ is an eigenvector of the Neumann Green's matrix \mathcal{G} . In the unit ball such special spot configurations occur when spots are located at vertices of a platonic solid concentric within the ball, when spots are equally spaced along an equator concentric within the ball, and for many of the equilibrium configurations of the ODE system for slow spot dynamics derived in section 4. When \mathbf{e} is not an eigenvector of \mathcal{G} , we show that there is an intricate imperfection-sensitive bifurcation structure of asymmetric quasi-equilibria for S near S_{cf} . For the case where $N = 2$, we provide a detailed analytical characterization of this imperfection-sensitive bifurcation behavior. We remark that a similar imperfection-sensitivity behavior for 2-D quasi-equilibrium spot patterns was first identified numerically in [18] for the Brusselator RD model, but no explicit asymptotic analysis of this behavior was given. Imperfection-sensitivity behavior, and the specific role of whether or not \mathbf{e} is an eigenvector of a certain Green's matrix, were not identified in the earlier analyses of [22], [25], [24], [23], [12], [2], and [14] of 2-D spot patterns for other RD models.

In section 3 we analyze the linear stability of N -spot symmetric quasi-equilibrium solutions to two distinct types of $\mathcal{O}(1)$ time-scale instabilities. From a numerical study of a local eigenvalue problem near each spot, associated with locally nonradial perturbations, in section 3.2 we show that the dominant spot shape-deforming instability is a mode $l = 2$ spherical harmonic, which we refer to as a peanut-splitting instability. This linear instability occurs when a spot source strength increases above the threshold $\Sigma_2 \approx 20.16$. We then verify numerically that this linear instability mechanism triggers a nonlinear spot self-replication event. In addition, for $N \geq 2$, a formal asymptotic analysis is used to derive an eigenvalue problem

associated with locally radially symmetric perturbations near each spot. To leading order as $\varepsilon \rightarrow 0$ we show that this linear competition instability, which preserves the sum of the spot amplitudes, is triggered through a zero-eigenvalue crossing when the common source strength S_c decreases below the threshold $S_{cf} \approx 4.52$, the common bifurcation point of asymmetric quasi-equilibria in the leading-order theory. This linear instability is found numerically to be the trigger of spot annihilation events. In summary, since $S_j = S_c + \mathcal{O}(\varepsilon)$ for $j = 1, \dots, N$, our leading-order asymptotic theory predicts that symmetric quasi-equilibrium N -spot patterns for $N \geq 2$ are linearly stable on an $\mathcal{O}(1)$ time-scale if and only if

$$(1.3) \quad A_{N,\min} < A < A_{N,\max}, \quad A_{N,\min} \equiv 56.798N\sqrt{D}/|\Omega|, \quad A_{N,\max} \equiv 253.33N\sqrt{D}/|\Omega|.$$

A spot self-replication event is triggered when the feed A is increased above the threshold $A_{N,\max}$, and a spot annihilation event due to overcrowding is triggered when A is decreased below $A_{N,\min}$.

Our hybrid analytical-numerical theory for the existence and linear stability of quasi-equilibrium patterns is validated for the unit ball with rather extensive full numerical simulations of the 3-D PDE system (1.2) using the finite-element package FlexPDE6 [6]. For the unit ball, the Neumann Green's function is known analytically (cf. [3]), making the comparison convenient. Because FlexPDE6 dynamically adapts the mesh according to the evolution of the solution, it is particularly useful for computing localized solutions in three dimensions. In our computations, FlexPDE6 used up to 40000 nodes with $\varepsilon = 0.03$.

Figure 1 illustrates the spot-splitting phenomenon. Here, the feed-rate A is ramped up very slowly, resulting in successive spot-replication events. The first such event occurs at $A \approx 60$, in excellent agreement with the theoretical prediction $A_{1,\max} = 60.48$. More generally, the asymptotic curve $A_{N,\max}$ is in excellent agreement with the numerics for a wide range of A ; see Figure 1 (right). We invite the interested reader to see full movies of the numerical solution here: M108121_01.mp4 [local/web 1.31MB], M108121_02.mp4 [local/web 1.25MB].

The overcrowding instability is illustrated in Figure 2, where the feed-rate A is ramped down very slowly, and the spots are eliminated one by one due to the competition instability. Again, good agreement between numerics and asymptotics is observed, as shown in Figure 2 (right), especially for small numbers of spots. For example, the theory predicts that two spots become unstable as A is decreased below $A_{2,\min} = 27.1$, whereas full numerics show that one of the two spots disappears at $A \approx 28$. The corresponding full movies of the numerical solution may be found here: M108121_03.mp4 [local/web 2.60MB], M108121_04.mp4 [local/web 2.47MB].

For the special case where \mathbf{e} is an eigenvector of the Neumann Green's matrix \mathcal{G} , in Main Result 3.1 we establish a more refined asymptotic prediction for the competition instability threshold that involves the smallest eigenvalue of \mathcal{G} in the subspace orthogonal to \mathbf{e} . In addition, in section 3.1 we formulate the linear stability problem for asymmetric quasi-equilibria and give some partial results for their stability.

When the stability condition (1.3) on the source strengths holds, in section 4 we show that the spot locations associated with an N -spot symmetric quasi-equilibrium evolve to a true steady-state configuration over a long $\mathcal{O}(\varepsilon^{-3})$ time-scale. To leading order in ε , in (4.18) of Main Result 4.2 we show that the slow spot dynamics satisfies an ODE system defined by a gradient flow of a certain discrete energy $\mathcal{H}(\mathbf{x}_1, \dots, \mathbf{x}_N)$, which involves the Neumann Green's

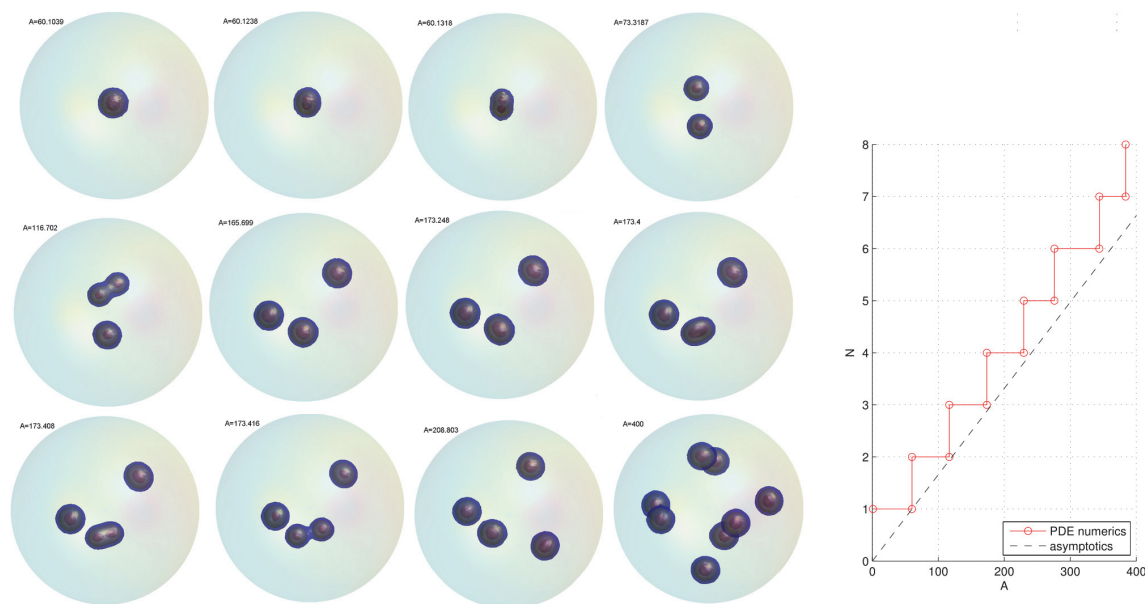


Figure 1. Self-replication events for (1.2) in the unit ball when slowly increasing the feed-rate A . Parameter values are $\varepsilon = 0.03$ and $D = 1$, while A is very slowly increased from 1 to 400 according to $A = 1 + 0.0036t$. Left: snapshots of solution for several values of A as shown. Right: the number of spots as a function of A , comparing the leading-order asymptotic theory given by $A_{N,\max}$ in (1.3) versus full numerics. Full movies of the numerical solution may be found here: M108121_01.mp4 [local/web 1.31MB], M108121_02.mp4 [local/web 1.25MB].

function and its regular part. Minima of this discrete energy are stable equilibrium points of this limiting ODE spot dynamics, and we explicitly identify certain such equilibrium spot configurations. A higher-order analysis, leading to the ODE dynamics (4.13) coupled to the constraints (2.34), shows that the slow spot dynamics consists of a weakly coupled system of differential algebraic equations (DAEs) in which the spot source strengths depend only weakly on the spot locations as $\varepsilon \rightarrow 0$.

In comparison, in a 2-D setting the dynamical characterization of slow spot dynamics consists of a DAE system that couples ODEs for the spot locations to a nonlinear algebraic system for the spot source strengths defined in terms of a Green's matrix, which depends on the overall spot configuration (cf. [12], [2], [18]). This DAE system of slow spot dynamics in two dimensions is rather strongly coupled, owing to the logarithmic gauge $\nu = \mathcal{O}(-1/\log \varepsilon)$. As a result of this strong coupling in two dimensions, spot self-replication events can be triggered intrinsically during the slow dynamics of a collection of spots whenever a particular spot source strength exceeds a critical value (cf. [12], [2], [14]). In contrast, in our 3-D setting where the spots have an asymptotically common source strength, with an error of only $\mathcal{O}(\varepsilon)$, such intrinsically triggered spot self-replication events do not typically occur for ε small. Instead, in three dimensions an external parameter such as the feed-rate, or the domain volume, needs to be increased dynamically in order to trigger spot self-replication events.

In section 4.1 we extend our asymptotic theory for constant A to the case of a spatially

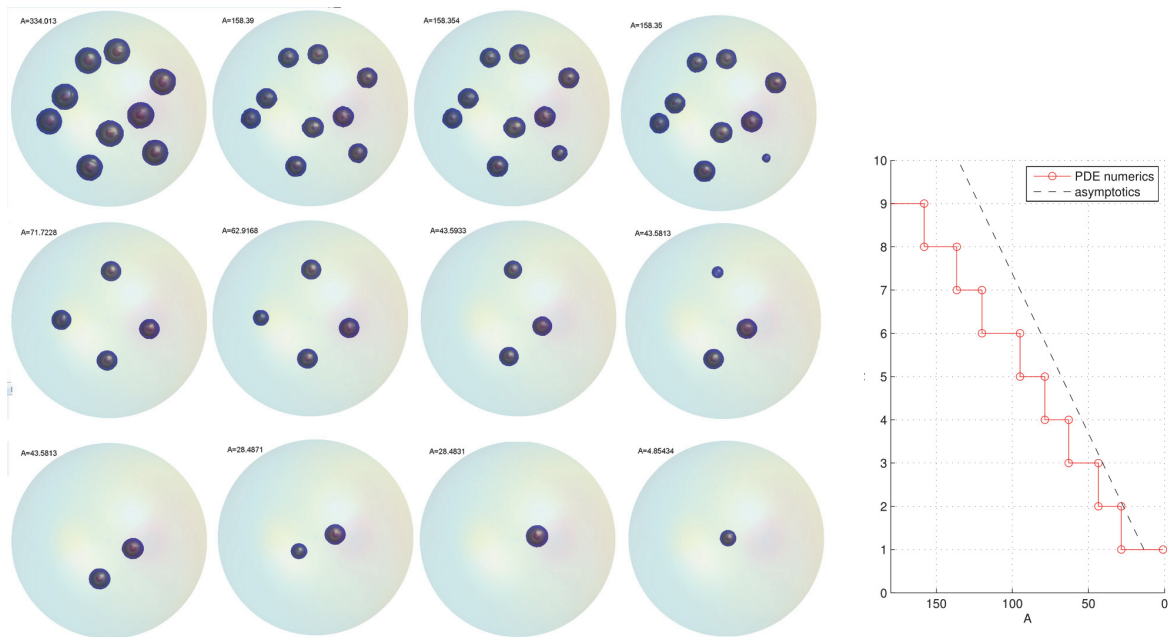


Figure 2. Coarsening when decreasing the feed-rate A . Parameter values are $\varepsilon = 0.03$ and $D = 1$, while A is very slowly decreased from 400 to 1 according to $A = 400 - 0.0036t$. Left: snapshots of solution for several values of A as shown. Right: the number of spots as a function of A , comparing leading-order asymptotic theory given by $A_{N,\min}$ in (1.3) versus full numerics. Full movies of the numerical solution may be found here: M108121_03.mp4 [local/web 2.60MB], M108121_04.mp4 [local/web 2.47MB].

variable feed, where $A = A(\mathbf{x})$ in (1.2b). For the linear stability theory, we find that the leading-order result (1.3) still holds provided that we replace A in (1.3) with \bar{A} , which denotes the spatial average of $A(\mathbf{x})$ over the domain. Moreover, to leading order in ε , the slow spot dynamics is characterized in Main Result 4.3 in terms of the discrete energy \mathcal{H} and an additional nonlocal term involving $A(\mathbf{x})$. In the unit ball, our ODEs characterizing slow spot dynamics are verified with full numerical FlexPDE6 simulations of (1.2). For a few specific choices of the variable feed-rate, we illustrate from our ODEs, and from full numerical PDE simulations, the effect of spot pinning, whereby a spot trajectory can be pinned to a new equilibrium state created by the nonuniform feed-rate. Finally, in section 5 we suggest a few open problems that warrant further study.

2. N -spot quasi-equilibria. In this section, we use the method of matched asymptotic expansions to construct an N -spot quasi-equilibrium solution to (1.2). In our analysis we assume that the feed $A > 0$ in (1.2b) is constant. The case of the spatially variable feed $A(\mathbf{x}) > 0$ is considered in section 4.1. We construct a pattern for which the spot solution is, to a first approximation, locally radially symmetric in an $\mathcal{O}(\varepsilon)$ region near the centers $\mathbf{x}_1, \dots, \mathbf{x}_N$ of the spots, where we assume $|\mathbf{x}_i - \mathbf{x}_j| = \mathcal{O}(1)$ for $i \neq j$. On an $\mathcal{O}(1)$ time-scale, we construct a quasi-equilibrium solution where the spot locations are, for $\varepsilon \rightarrow 0$, stationary in time. In section 4, we will show that the spot dynamics is slow and occurs on the long time-scale $t = \mathcal{O}(\varepsilon^{-3}) \gg 1$.

In the inner region near the j th spot, we introduce the local variables

$$(2.1) \quad \mathbf{y} = \varepsilon^{-1}(\mathbf{x} - \mathbf{x}_j), \quad v(\mathbf{x}_j + \varepsilon\mathbf{y}) = \sqrt{D} [V_{j0}(\rho) + \varepsilon V_{j1} + \cdots], \\ u(\mathbf{x}_j + \varepsilon\mathbf{y}) = \frac{1}{\sqrt{D}} [U_{j0}(\rho) + \varepsilon U_{j1} + \cdots],$$

where $\rho = |\mathbf{y}|$. Upon substituting (2.1) into (1.2) we obtain, to leading order on $0 < \rho < \infty$, that

$$(2.2a) \quad \Delta_\rho V_{j0} - V_{j0} + U_{j0} V_{j0}^2 = 0, \quad V_{j0}'(0) = 0, \quad V_{j0} \rightarrow 0, \quad \text{as } \rho \rightarrow \infty,$$

$$(2.2b) \quad \Delta_\rho U_{j0} - U_{j0} V_{j0}^2 = 0, \quad U_{j0}'(0) = 0,$$

where $\Delta_\rho V_{j0} \equiv V_{j0}'' + 2\rho^{-1}V_{j0}'$. The linear $-V_{j0}$ term in (2.2a) allows us to impose an exponential decay condition at infinity for V_{j0} , whereas the far-field behavior of U_{j0} must be proportional to the free-space Green's function for the Laplacian in three dimensions. As such, in terms of some unknown source strength S_j , we impose $\lim_{\rho \rightarrow \infty} \rho^2 \partial_\rho U_{j0}|_{\rho=\rho_0} = S_j$, so that the far-field behavior for U_{j0} is

$$(2.2c) \quad U_{j0} \sim \mu_j - S_j/\rho + \cdots, \quad \text{as } \rho \rightarrow \infty,$$

where $\mu_j = \mu_0(S_j)$ must be computed numerically from (2.2). From (2.2b), we readily obtain the identity

$$(2.3) \quad S_j = \int_0^\infty U_{j0} V_{j0}^2 \rho^2 d\rho.$$

Next, we obtain an asymptotic solution for u in the outer region in terms of the Neumann Green's function. We first note that $v \sim 0$ in the outer region, and that from (2.1) and (2.3) we can express the term $\varepsilon^{-3}uv^2$ in (1.2b) in the sense of distributions as

$$(2.4) \quad \varepsilon^{-3}uv^2 \rightarrow 4\pi\sqrt{D} \sum_{j=1}^N \left(\int_0^\infty U_{j0} V_{j0}^2 \rho^2 d\rho \right) \delta(\mathbf{x} - \mathbf{x}_j) = 4\pi\sqrt{D} \sum_{j=1}^N S_j \delta(\mathbf{x} - \mathbf{x}_j).$$

Therefore, from (1.2b), the quasi-equilibrium solution for u in the outer region satisfies

$$(2.5) \quad \frac{1}{\varepsilon} \Delta u + \frac{A}{D} \sim \frac{4\pi}{\sqrt{D}} \sum_{j=1}^N S_j \delta(\mathbf{x} - \mathbf{x}_j), \quad \mathbf{x} \in \Omega; \quad \partial_n u = 0, \quad \mathbf{x} \in \partial\Omega.$$

This expression suggests an expansion for u in the form

$$(2.6) \quad u \sim u_0 + \varepsilon u_1 + \varepsilon^2 u_2 + \cdots,$$

where u_0 is an unknown global constant, and where u_1 satisfies

$$(2.7) \quad \Delta u_1 + \frac{A}{D} = \frac{4\pi}{\sqrt{D}} \sum_{j=1}^N S_j \delta(\mathbf{x} - \mathbf{x}_j), \quad \mathbf{x} \in \Omega; \quad \partial_n u_1 = 0, \quad \mathbf{x} \in \partial\Omega.$$

By applying the divergence theorem to (2.7), we obtain the solvability condition

$$(2.8) \quad \sum_{j=1}^N S_j = \frac{A|\Omega|}{4\pi\sqrt{D}}.$$

Then, we write the solution to (2.7) as

$$(2.9) \quad u_1 = -\frac{4\pi}{\sqrt{D}} \sum_{i=1}^N S_i G(\mathbf{x}; \mathbf{x}_i) + \bar{u}_1,$$

for some unknown constant \bar{u}_1 , where $G(\mathbf{x}, \boldsymbol{\xi})$ is the unique Neumann Green's function satisfying

$$(2.10a) \quad \Delta G = \frac{1}{|\Omega|} - \delta(\mathbf{x} - \boldsymbol{\xi}), \quad \mathbf{x} \in \Omega; \quad \partial_n G = 0, \quad \mathbf{x} \in \partial\Omega,$$

$$(2.10b) \quad G(\mathbf{x}; \boldsymbol{\xi}) = \frac{1}{4\pi|\mathbf{x} - \boldsymbol{\xi}|} + R(\mathbf{x}; \boldsymbol{\xi}), \quad \text{as } \mathbf{x} \rightarrow \boldsymbol{\xi}; \quad \int_{\Omega} G \, d\mathbf{x} = 0,$$

where $R(\mathbf{x}; \boldsymbol{\xi})$ is smooth. In (2.10b), $R(\boldsymbol{\xi}; \boldsymbol{\xi})$ is called the regular part of G at the singularity $\mathbf{x} = \boldsymbol{\xi}$. For the special case where Ω is the unit ball, the Neumann Green's function is given explicitly by (cf. [3])

$$(2.11a) \quad G(\mathbf{x}; \boldsymbol{\xi}) = \frac{1}{4\pi|\mathbf{x} - \boldsymbol{\xi}|} + \frac{1}{4\pi|\mathbf{x}||\mathbf{x}' - \boldsymbol{\xi}|} + \frac{1}{4\pi} \log \left(\frac{2}{1 - \mathbf{x} \cdot \boldsymbol{\xi} + |\mathbf{x}||\mathbf{x}' - \boldsymbol{\xi}|} \right) + \frac{1}{8\pi} (|\mathbf{x}|^2 + |\boldsymbol{\xi}|^2) - \frac{7}{10\pi}.$$

Here $\mathbf{x}' = \mathbf{x}/|\mathbf{x}|^2$ is the image point to \mathbf{x} outside the unit ball, and \cdot denotes the dot product. To calculate $R(\boldsymbol{\xi}; \boldsymbol{\xi})$ from (2.11a) we take the limit of $G(\mathbf{x}, \boldsymbol{\xi})$ as $\mathbf{x} \rightarrow \boldsymbol{\xi}$ and extract the nonsingular part of the resulting expression. We readily obtain that

$$(2.11b) \quad R(\boldsymbol{\xi}; \boldsymbol{\xi}) = \frac{1}{4\pi(1 - |\boldsymbol{\xi}|^2)} - \frac{1}{4\pi} \log(1 - |\boldsymbol{\xi}|^2) + \frac{|\boldsymbol{\xi}|^2}{4\pi} - \frac{7}{10\pi}.$$

Next, by using (2.6) with (2.9) and (2.10b), we obtain that the local behavior of u near \mathbf{x}_j is

$$(2.12) \quad u \sim u_0 + \varepsilon \left[-\frac{S_j}{\sqrt{D}|\mathbf{x} - \mathbf{x}_j|} - \frac{4\pi}{\sqrt{D}} \left(S_j R_{jj} + \sum_{\substack{i=1 \\ i \neq j}}^N S_i G_{ji} \right) + \bar{u}_1 \right], \quad \text{as } \mathbf{x} \rightarrow \mathbf{x}_j.$$

Here, we have defined $R_{jj} \equiv R(\mathbf{x}_j; \mathbf{x}_j)$ and $G_{ji} \equiv G(\mathbf{x}_j; \mathbf{x}_i)$. Matching the local behavior (2.12) to the far-field behavior (2.2c) of the inner solution U_{j0} , we find to leading order that

$$(2.13) \quad \mu_j = \sqrt{D}u_0, \quad j = 1, \dots, N,$$

while the singularity behavior matches by construction. Because the spot strengths are determined in terms of μ_j , the simplest N -spot pattern is one in which all spots have a common

source strength $S_j = S_c$ for $j = 1, \dots, N$, independent of their locations. From (2.8), we obtain that this common source strength is

$$(2.14) \quad S_c = \frac{A|\Omega|}{4\pi N\sqrt{D}}.$$

We refer to such a pattern as ‘‘symmetric.’’ This result is analogous to that for the mean first passage time (MFPT) for a narrow capture problem in a 3-D domain with N small identical traps [3], where the leading-order average MFPT is independent of the locations of the traps in the domain.

A symmetric quasi-equilibrium pattern of N spots is then characterized to leading order by

$$(2.15) \quad v_{qe} \sim \sqrt{D} \sum_{i=1}^N V_c(\varepsilon^{-1}|\mathbf{x} - \mathbf{x}_i|), \quad u_{qe} \sim \frac{1}{\sqrt{D}}\mu_0 + \varepsilon \left(-\frac{4\pi S_c}{\sqrt{D}} \sum_{i=1}^N G(\mathbf{x}; \mathbf{x}_i) + \bar{u}_1 \right),$$

where \bar{u}_1 is a constant to be determined below in section 2.1 by a higher-order matching procedure. Here $V_c(\rho)$ and $\mu_0 = \mu_0(S)$, with $S = S_c$, are determined by the following radially symmetric core problem on $0 < \rho < \infty$:

$$(2.16a) \quad \Delta_\rho V_c - V_c + U_c V_c^2 = 0, \quad V_c'(0) = 0, \quad V_c \rightarrow 0, \quad \text{as } \rho \rightarrow \infty,$$

$$(2.16b) \quad \Delta_\rho U_c - U_c V_c^2 = 0, \quad U_c'(0) = 0, \quad U_c \sim \mu_0 - \frac{S}{\rho}, \quad \text{as } \rho \rightarrow \infty.$$

In the inner region near \mathbf{x}_j , we have that v_{qe} and u_{qe} are given to leading order by

$$(2.17) \quad v_{qe} \sim \sqrt{D} V_c(\varepsilon^{-1}|\mathbf{x} - \mathbf{x}_j|), \quad u_{qe} \sim \frac{1}{\sqrt{D}} U_c(\varepsilon^{-1}|\mathbf{x} - \mathbf{x}_j|).$$

Upon solving the BVP (2.16) using numerical continuation, we plot μ_0 in terms of the strength S in Figure 3(a). The fold point at $(S_{cf}, \mu_{0f}) \approx (4.52, 5.78)$ divides $\mu_0(S)$ into a left and a right branch as shown in Figure 3(a). In addition, in Figure 3(b),(c) we plot V_c and U_c versus ρ , respectively, for a few values of S . We observe from Figure 3(b) that V_c has a volcano-shaped profile, characterized by a maximum not at $\rho = 0$, when $S \geq 18.7$.

We can determine the limiting asymptotics as $S \rightarrow 0$ for the curve $\mu_0(S)$ by seeking a perturbation solution of (2.16) as $S \rightarrow 0$. We readily derive for $S \rightarrow 0$ that

$$(2.18) \quad U_c \sim \frac{b}{S} \left(1 + \frac{S^2}{b^2} (\mu_1 + U_{c1}) + \dots \right), \quad V_c \sim \frac{S}{b} \left(w + \frac{S^2}{b^2} (-\mu_1 w + V_{c1}) \right),$$

and that $\mu_0(S)$ for $S \ll 1$ has the limiting asymptotics

$$(2.19) \quad \mu_0 \sim \frac{b}{S} \left(1 + \frac{S^2}{b^2} \mu_1 + \dots \right); \quad b \equiv \int_0^\infty \rho^2 w^2 d\rho, \quad \mu_1 \equiv b^{-1} \int_0^\infty \rho^2 V_{c1} d\rho.$$

Here $w(\rho)$ is the unique ground-state solution of $\Delta_\rho w - w + w^2 = 0$ with $w(0) > 0$ and $\lim_{\rho \rightarrow \infty} w = 0$, while $U_{c1}(\rho)$ and $V_{c1}(\rho)$ are the unique solutions on $0 < \rho < \infty$ to

$$(2.20a) \quad \mathcal{L}V_{c1} \equiv \Delta_\rho V_{c1} - V_{c1} + 2wV_{c1} = -w^2 U_{c1}; \quad V_{c1}'(0) = 0, \quad \lim_{\rho \rightarrow \infty} V_{c1} = 0,$$

$$(2.20b) \quad \Delta_\rho U_{c1} = w^2; \quad U_{c1}'(0) = 0, \quad U_{c1} \sim -b/\rho, \quad \text{as } \rho \rightarrow \infty.$$

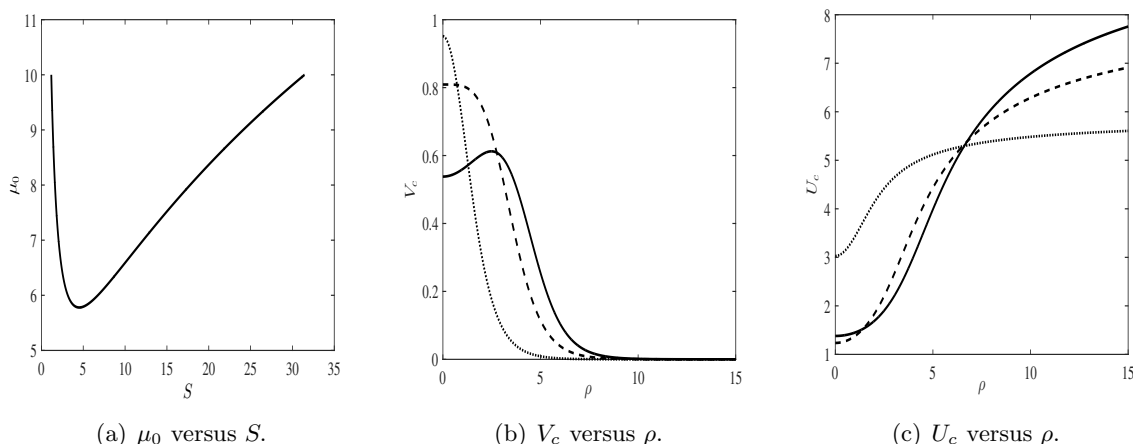


Figure 3. In (a), we plot the relationship $\mu_0 = \mu_0(S)$ as obtained from a numerical solution of the core problem (2.16). The fold point at $(S_{cf}, \mu_{0f}) \approx (4.52, 5.78)$ divides $\mu_0(S)$ into a left and a right branch. In (b), we plot V_c versus $\rho = |\mathbf{y}|$ for $S = 3.67$ (dotted line), $S = 18.7$ (dashed line), and $S = 29.1$ (solid line). For $S \gtrsim 18.7$, the profile is volcano shaped so that the maximum of V_c occurs at $\rho > 0$. When $S \lesssim 18.7$, the maximum of V_c is at $\rho = 0$. In (c), we show the corresponding profiles for $U_c(\rho)$.

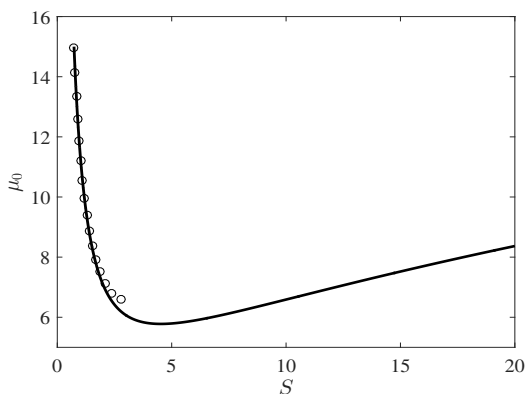


Figure 4. Comparison of the asymptotic result (2.19) for μ_0 for small S (discrete points) with the numerical result (solid curve) computed from (2.16). In (2.19) we use $b \approx 10.43$ and $\mu_1 \approx 10.67$. The asymptotic result agrees well on $0 < S < 3$, with the minimum of the μ_0 versus S graph occurring at $S_{cf} \approx 4.52$.

By solving for w and the pair (U_{c1}, V_{c1}) numerically, we estimate that $b \approx 10.43$ and $\mu_1 \approx 10.67$. In Figure 4 we show that the asymptotic result (2.19) agrees very closely with the corresponding numerical result for most of the left branch of the μ_0 -versus- S curve of Figure 3(a).

For a given $\mu_0 > \mu_{0f}$, the multivalued nature of $S(\mu_0)$ in Figure 3(a) gives rise to the possibility of “asymmetric” patterns consisting of N_ℓ spots with strength S_ℓ on the left branch

and N_r spots with strength S_r on the right branch. Such a pattern takes the form

$$(2.21a) \quad v_{qe} \sim \sqrt{D} \sum_{i=1}^{N_\ell} V_{cl}(\varepsilon^{-1}|\mathbf{x} - \mathbf{x}_i|) + \sqrt{D} \sum_{i=1}^{N_r} V_{cr}(\varepsilon^{-1}|\mathbf{x} - \mathbf{x}_i|),$$

$$(2.21b) \quad u_{qe} \sim \frac{\mu_0}{\sqrt{D}} + \varepsilon \left(-\frac{4\pi S_\ell}{\sqrt{D}} \sum_{i=1}^{N_\ell} G(\mathbf{x}; \mathbf{x}_i) - \frac{4\pi S_r}{\sqrt{D}} \sum_{i=1}^{N_r} G(\mathbf{x}; \mathbf{x}_i) + \bar{u}_1 \right),$$

where the pairs (V_{cl}, U_{cl}) and (V_{cr}, U_{cr}) are the solutions to (2.16) with $U_{cl} \sim \mu_0 - S_\ell/\rho$ as $\rho \rightarrow \infty$, and $U_{cr} \sim \mu_0 - S_r/\rho$ as $\rho \rightarrow \infty$, respectively. For given positive integers N_ℓ and N_r , with $N = N_\ell + N_r$, the two source strengths S_ℓ and S_r for the leading-order asymmetric pattern must be determined from the nonlinear algebraic problem

$$(2.22) \quad N_\ell S_\ell + N_r S_r = \frac{A|\Omega|}{4\pi\sqrt{D}}, \quad \mu_0(S_\ell) = \mu_0(S_r), \quad \text{where } S_\ell < S_{cf} < S_r.$$

For $N = 2$ and $N = 4$, in Figure 5 we plot the symmetric and asymmetric solution branches, as computed numerically from (2.22) using MATCONT [5]. From these figures we observe that the leading-order asymptotic theory predicts that the asymmetric branches bifurcate from the symmetric solution branch at $S_{cf} \approx 4.52$.

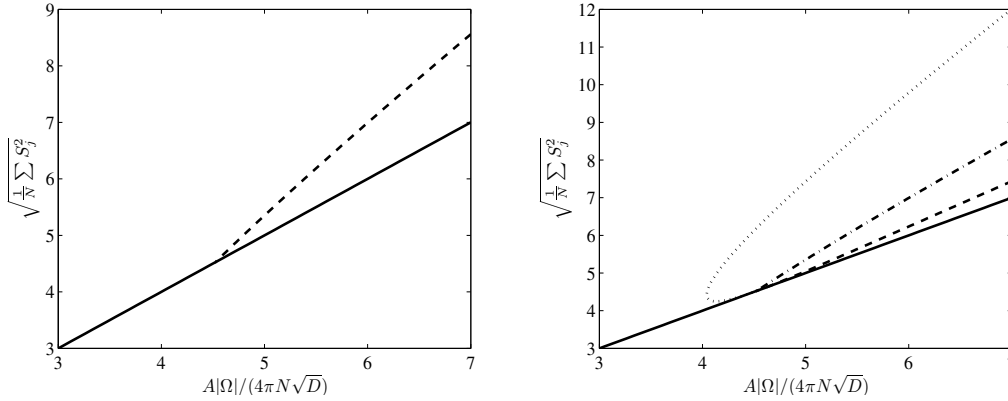


Figure 5. Bifurcation diagram of $\sqrt{N^{-1} \sum_i S_{i\varepsilon}^2}$ versus $A|\Omega|/(4\pi N\sqrt{D})$ computed using MATCONT [5] from the leading-order problem (2.22) for $D = 0.1$ and $\varepsilon = 0.05$ for $N = 2$ spots (left panel) and for $N = 4$ spots (right panel). The heavy solid curve in each panel is the symmetric solution branch. In the left panel, the dashed curve represents the asymmetric branch. In the right panel the labeling of the curves is as follows: $N_r = 3$ and $N_\ell = 1$ (dashed curve); $N_r = N_\ell = 2$ (dashed-dotted curve); $N_r = 1$ and $N_\ell = 3$ (dotted curve). The leading-order theory predicts that the asymmetric branches bifurcate from a common point.

2.1. Refined asymptotic theory. For the symmetric quasi-equilibrium pattern constructed above we now perform a higher-order matching procedure to determine the constant \bar{u}_1 in (2.15). This analysis is also needed in section 4 in our derivation of slow spot dynamics.

With $u_0 = \mu_0/\sqrt{D}$ and $S = S_c$, we first write the local behavior (2.12) in terms of inner variables as

$$(2.23) \quad u \sim \frac{1}{\sqrt{D}} \left(\mu_0 - \frac{S_c}{\rho} \right) + \varepsilon \left[-\frac{4\pi S_c}{\sqrt{D}} (\mathcal{G}\mathbf{e})_j + \bar{u}_1 \right] + \dots, \quad \text{as } \mathbf{x} \rightarrow \mathbf{x}_j.$$

Here $\mathbf{e} \equiv (1, \dots, 1)^T$, while \mathcal{G} is the $N \times N$ symmetric Neumann Green's matrix with matrix entries $(\mathcal{G})_{ij} = G(\mathbf{x}_j; \mathbf{x}_i)$ for $i \neq j$ and $(\mathcal{G})_{jj} = R(\mathbf{x}_j; \mathbf{x}_j)$.

To account for the $\mathcal{O}(\varepsilon)$ correction to the singularity behavior in (2.23), we need the higher-order terms U_{j1} and V_{j1} in the inner expansion as introduced in (2.1). Upon substituting (2.1) into (1.2), we obtain in matrix form that $\mathbf{W}_1 = (V_{j1}, U_{j1})^T$ satisfies

$$(2.24a) \quad \Delta_\rho \mathbf{W}_1 + \mathcal{M} \mathbf{W}_1 = 0, \quad 0 < \rho < \infty,$$

$$(2.24b) \quad \mathbf{W}'_1(0) = (0, 0)^T; \quad \mathbf{W}_1 \sim (0, \alpha_j)^T, \quad \text{as } \rho \rightarrow \infty,$$

where α_j and the 2×2 matrix \mathcal{M} are defined by

$$(2.24c) \quad \alpha_j \equiv -4\pi S_c (\mathcal{G}\mathbf{e})_j + \bar{u}_1 \sqrt{D}, \quad \mathcal{M} \equiv \begin{pmatrix} -1 + 2U_c V_c & V_c^2 \\ -2U_c V_c & -V_c^2 \end{pmatrix}.$$

We can readily identify the solution to (2.24) by differentiating the core problem (2.16) with respect to S . For $S \neq S_{cf}$, we obtain that

$$(2.25) \quad V_{j1} = \frac{\alpha_j}{\mu'_0(S)} \partial_S V_c, \quad U_{j1} = \frac{\alpha_j}{\mu'_0(S)} \partial_S U_c.$$

Therefore, provided that $S_c \neq S_{cf}$, we have for $S = S_c$ that

$$(2.26) \quad U_{j1} \sim \alpha_j - \frac{\alpha_j}{\mu'_0(S_c)\rho}, \quad \text{as } \rho \rightarrow \infty, \quad \text{and} \quad \int_0^\infty (2U_c V_c V_{j1} + V_c^2 U_{j1}) \rho^2 d\rho = \frac{\alpha_j}{\mu'_0(S_c)}.$$

Next, we proceed to one higher order in the outer region. In the sense of distributions, and upon using the integral identity in (2.26), we get as $\varepsilon \rightarrow 0$ that

$$(2.27) \quad \varepsilon^{-3} uv^2 \rightarrow 4\pi \sqrt{D} \sum_{j=1}^N \left[S_c + \frac{\varepsilon \alpha_j}{\mu'_0(S_c)} \right] \delta(\mathbf{x} - \mathbf{x}_j).$$

By using (2.27) in (1.2b), we obtain that the term u_2 in the outer expansion (2.6) satisfies

$$(2.28) \quad \Delta u_2 = \frac{4\pi}{\sqrt{D} \mu'_0(S_c)} \sum_{j=1}^N \alpha_j \delta(\mathbf{x} - \mathbf{x}_j), \quad \mathbf{x} \in \Omega; \quad \partial_n u_2 = 0, \quad \mathbf{x} \in \partial\Omega.$$

The solvability condition for (2.28) is that $\sum_{j=1}^N \alpha_j = 0$. Upon using (2.24c) for α_j , we determine \bar{u}_1 as

$$(2.29) \quad \bar{u}_1 = \frac{4\pi S_c}{N \sqrt{D}} (\mathbf{e}^T \mathcal{G} \mathbf{e}).$$

Then, by solving (2.28) for u_2 up to a constant, and by using (2.15) and (2.29), we obtain that the outer expansion for a symmetric N -spot quasi-equilibrium solution is

$$(2.30) \quad u_{qe} \sim \frac{\mu_0}{\sqrt{D}} + \frac{4\pi \varepsilon S_c}{\sqrt{D}} \left(-\sum_{i=1}^N G(\mathbf{x}; \mathbf{x}_i) + \frac{\mathbf{e}^T \mathcal{G} \mathbf{e}}{N} \right) - \frac{4\pi \varepsilon^2}{\sqrt{D}} \left(\frac{4\pi S_c}{\mu'_0(S_c)} \right) \sum_{i=1}^N \left[\frac{\mathbf{e}^T \mathcal{G} \mathbf{e}}{N} - (\mathcal{G}\mathbf{e})_i \right] G(\mathbf{x}; \mathbf{x}_i) + \varepsilon^2 \bar{u}_2 + \dots$$

To illustrate (2.30), we let $N = 1$, Ω be the unit ball, and take $\mathbf{x}_1 = \mathbf{0}$, so that the spot is at the center of the ball. Then we use the explicit Green’s function (2.11) to obtain from (2.30) that

$$u_{qe} \sim \frac{\mu_0}{\sqrt{D}} - \frac{\varepsilon S_c}{\sqrt{D}} \left(\frac{r^2}{2} + \frac{1}{r} \right) + \mathcal{O}(\varepsilon^2), \quad S_c = \frac{A}{3\sqrt{D}},$$

where $r = |\mathbf{x}|$, so that on the domain boundary where $r = 1$ we get

$$(2.31) \quad u_{qe} = \frac{\mu_0}{\sqrt{D}} - \frac{3\varepsilon S_c}{2\sqrt{D}}, \quad \mathbf{x} \in \partial\Omega.$$

For this radially symmetric setting, we can solve for the steady-state of (1.2) numerically and then compare with the asymptotic result (2.31). The comparison of u_{qe} on the domain boundary versus ε in Figure 6 shows that the asymptotic result is very accurate even when ε is only moderately small.

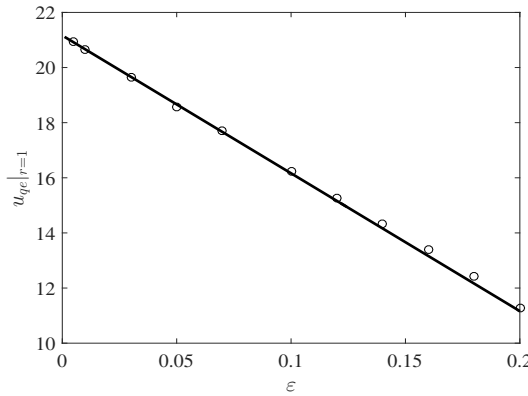


Figure 6. Comparison of asymptotic result (2.31) (solid curve) and full numerical result computed from the steady-state of (1.2) (discrete points) for u corresponding to a one spot solution centered at the origin in the unit ball. The parameters are $A = 10$ and $D = 0.1$.

Finally, we provide an alternative analysis to construct an N -spot quasi-equilibrium solution, which is needed in sections 3 and 4. In this approach, we allow the source strength S_j in (2.2c) to depend weakly on ε , and so we write $U_{j\varepsilon}, V_{j\varepsilon}$ as the solution to (2.2) for which $U_{j\varepsilon} \sim \mu_j - S_{j\varepsilon}/\rho$ as $\rho \rightarrow \infty$, where $\mu_j \equiv \mu_0(S_{j\varepsilon})$. By proceeding as in (2.4) and (2.5), we obtain that the outer solution satisfies

$$(2.32) \quad \Delta u + \frac{\varepsilon A}{D} \sim \frac{4\pi\varepsilon}{\sqrt{D}} \sum_{j=1}^N S_{j\varepsilon} \delta(\mathbf{x} - \mathbf{x}_j), \quad \mathbf{x} \in \Omega; \quad \partial_n u = 0, \quad \mathbf{x} \in \partial\Omega.$$

Instead of expanding u as a power series in ε as in (2.6), we solve (2.32) exactly to obtain

$$(2.33) \quad u = \xi - \frac{4\pi\varepsilon}{\sqrt{D}} \sum_{i=1}^N S_{i\varepsilon} G(\mathbf{x}; \mathbf{x}_i), \quad \sum_{i=1}^N S_{i\varepsilon} = \frac{A|\Omega|}{4\pi\sqrt{D}},$$

where ξ is a constant and G satisfies (2.10). By matching the local behavior of the outer solution u as $\mathbf{x} \rightarrow \mathbf{x}_j$ with the far-field behavior $u_j = D^{-1/2}U_{j\varepsilon} \sim D^{-1/2}(\mu_j - S_{j\varepsilon}/\rho)$ of the j th inner solution, where $\mu_j \equiv \mu_0(S_{j\varepsilon})$, we obtain that $S_{j\varepsilon}$ for $j = 1, \dots, N$, and the constant ξ must satisfy the $(N + 1)$ -dimensional weakly coupled nonlinear algebraic system

$$(2.34) \quad \xi - \frac{4\pi\varepsilon}{\sqrt{D}}(\mathcal{G}\mathbf{S})_j = \frac{\mu_0(S_{j\varepsilon})}{\sqrt{D}}, \quad j = 1, \dots, N; \quad \sum_{j=1}^N S_{j\varepsilon} = \frac{A|\Omega|}{4\pi\sqrt{D}}.$$

Here $\mu_0(S_{j\varepsilon})$ is to be computed from the core problem (2.2), $\mathbf{S} \equiv (S_{1\varepsilon}, \dots, S_{N\varepsilon})^T$, and \mathcal{G} is the symmetric Neumann Green's matrix with matrix entries $(\mathcal{G})_{ij} = G(\mathbf{x}_j; \mathbf{x}_i)$ for $i \neq j$ and $(\mathcal{G})_{jj} = R(\mathbf{x}_j; \mathbf{x}_j)$. It is readily shown from (2.34) that a two-term expansion for ξ and $S_{j\varepsilon}$ is

$$(2.35) \quad S_{j\varepsilon} \sim S_c + \frac{4\pi\varepsilon S_c}{\mu'_0(S_c)} \left(\frac{\mathbf{e}^T \mathcal{G} \mathbf{e}}{N} - (\mathcal{G} \mathbf{e})_j \right) + \dots, \quad j = 1, \dots, N, \\ \xi \sim \frac{\mu_0(S_c)}{\sqrt{D}} + \frac{4\pi\varepsilon}{\sqrt{DN}} S_c \mathbf{e}^T \mathcal{G} \mathbf{e} + \dots,$$

provided that $S_c \neq S_{cf}$. Upon substituting this result into (2.33) we recover our previous result (2.30) obtained from a more conventional power series representation of the outer solution.

An important special case of (2.34) occurs when the spot locations are aligned so that $\mathbf{e} = (1, \dots, 1)^T$ is an eigenvector of the Green's matrix \mathcal{G} . In particular, assume that $\mathcal{G} \mathbf{e} = k_1 \mathbf{e}$ for some eigenvalue k_1 . Then (2.34) has a solution with $\mathbf{S} = S_c \mathbf{e}$ for any $\varepsilon > 0$, for which

$$(2.36) \quad \xi = \frac{4\pi\varepsilon}{\sqrt{D}} S_c k_1 + \frac{\mu_0(S_c)}{\sqrt{D}}, \quad S_c \equiv \frac{A|\Omega|}{4\pi N \sqrt{D}}.$$

Therefore, when $\mathcal{G} \mathbf{e} = k_1 \mathbf{e}$, there is a common source strength solution to (2.34) that is precisely the same as that for the leading-order solution in (2.14). For this special case, we readily identify that $\alpha_j = 0$ in (2.24c) so that $U_{j1} = V_{j1} = 0$ from (2.25). As a consequence, we have $U_{j\varepsilon} = U_c + \mathcal{O}(\varepsilon^2)$ and $V_{j\varepsilon} = V_c + \mathcal{O}(\varepsilon^2)$, which is used in section 3 in our linear stability analysis.

For $N = 4$, we now illustrate the solution structure to the nonlinear algebraic system (2.34) in the unit ball for both the situation where \mathbf{e} is an eigenvector of \mathcal{G} and when this condition does not hold. We first place the spots at the vertices of a tetrahedron at a distance $r_0 = 0.564$ from the origin, with one spot at the north pole. From Table 1, as discussed in section 4, this configuration, for which \mathbf{e} is an eigenvector of \mathcal{G} , is a true equilibrium state for (1.2). We then solve (2.34) numerically using MATCONT [5] for $D = 0.1$ and $\varepsilon = 0.05$ to compute both the symmetric and asymmetric branches of solutions as the parameter A is varied. The results shown in Figure 7(a) indicate that all the asymmetric solutions (see caption for branch identification) bifurcate from the symmetric branch (heavy solid line) at the common value predicted from our theory. However, in contrast, if we then perturb the spot at the north pole so that \mathbf{e} is no longer an eigenvector of \mathcal{G} , we observe from Figure 7(b) an imperfection-sensitivity phenomenon whereby the asymmetric solution branches now exhibit a saddle-node structure, and the bifurcation point from the symmetric branch as predicted by the leading-order theory does not persist under the ε -perturbation induced by (2.34). In

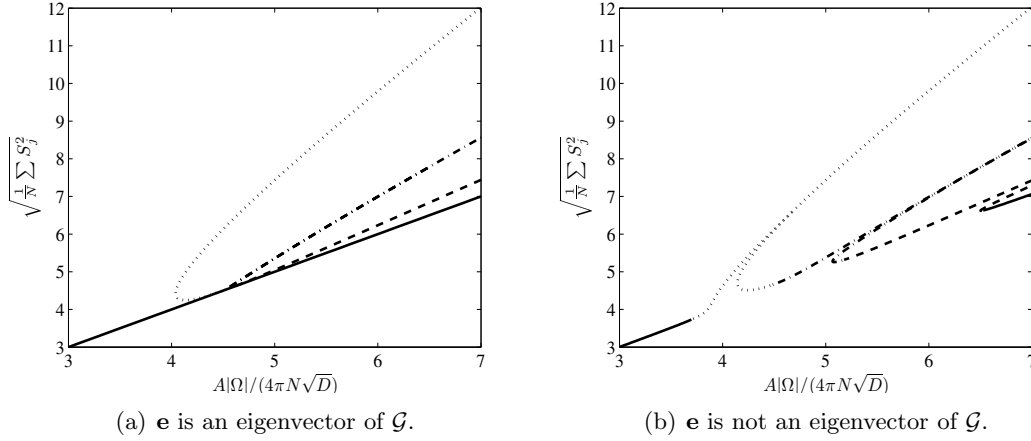


Figure 7. (a) Bifurcation diagram of $\sqrt{N^{-1} \sum_i S_{i\varepsilon}^2}$ versus $A|\Omega|/(4\pi N\sqrt{D})$, computed from (2.34) using MATCONT [5], for $D = 0.1$ and $\varepsilon = 0.05$ when $N = 4$ spots are placed at the vertices of a tetrahedron of radius $r_0 = 0.564$ concentric with the unit ball where $|\Omega| = 4\pi/3$. For this case where \mathbf{e} is an eigenvector of \mathcal{G} all three asymmetric branches of quasi-equilibria bifurcate from the common value (4.52, 4.52) as expected by the theory. The curves are defined with respect to the left and right branches of $\mu_0(S)$ in Figure 3(a): symmetric branch (solid curve); 3 right 1 left (dashed curve); 2 right 2 left (dashed-dotted curve); 1 right 3 left (dotted curve). (b) Same plot and parameter values as in (a) except that the spot at the north pole for the tetrahedron is moved to $r_0(0, \sin(\pi/6), \cos(\pi/6))$ with $r_0 = 0.564$. In this case there is an imperfection sensitivity of the asymmetric solution branches, and the bifurcation point from the symmetric branch predicted by the leading-order theory does not persist under the ε -perturbation. Some solution branches corresponding to permutations of the asymmetric patterns have been omitted in (b) for clarity.

a 2-D context, a similar imperfection-sensitivity behavior was first observed in [18] for spot patterns of the Brusselator RD model on the surface of the unit ball. In Figure 7(b), the heavy solid curves indicate solution branches of (2.34) where the strengths $S_{j\varepsilon}$ satisfy either $S_{j\varepsilon} < S_{cf}$ for all j or $S_{j\varepsilon} > S_{cf}$ for all j . The other curves indicate solutions that consist of strengths both smaller and larger than S_{cf} (see figure caption for details).

For the case of $N = 2$ spots for which \mathbf{e} is not an eigenvector of \mathcal{G} we now provide an asymptotic theory to analytically characterize the imperfection sensitivity as shown in Figure 8, which was obtained by solving (2.34) numerically using MATCONT [5]. The heavy solid curves indicate solutions of (2.34) in which $S_1, S_2 < S_{cf}$ or $S_1, S_2 > S_{cf}$, while the dashed curves indicate asymmetric solutions where $S_1 < S_{cf}$ and $S_2 > S_{cf}$ and vice versa. For $N = 2$, we eliminate ξ in (2.34) to obtain

$$(2.37) \quad S_1 + S_2 = \frac{A|\Omega|}{4\pi\sqrt{D}}, \quad \mu_0(S_1) - \mu_0(S_2) = -4\pi\varepsilon [R_{11}S_1 - R_{22}S_2 + (S_2 - S_1)G_{12}],$$

where we have relabeled $S_1 = S_{1\varepsilon}$ and $S_2 = S_{2\varepsilon}$ for simplicity. We now introduce a detuning parameter δ that measures how close we are to the critical value S_{cf} , so that

$$(2.38) \quad \frac{A|\Omega|}{4\pi(2)\sqrt{D}} = S_{cf} + \frac{\delta}{2}, \quad \delta \ll 1,$$

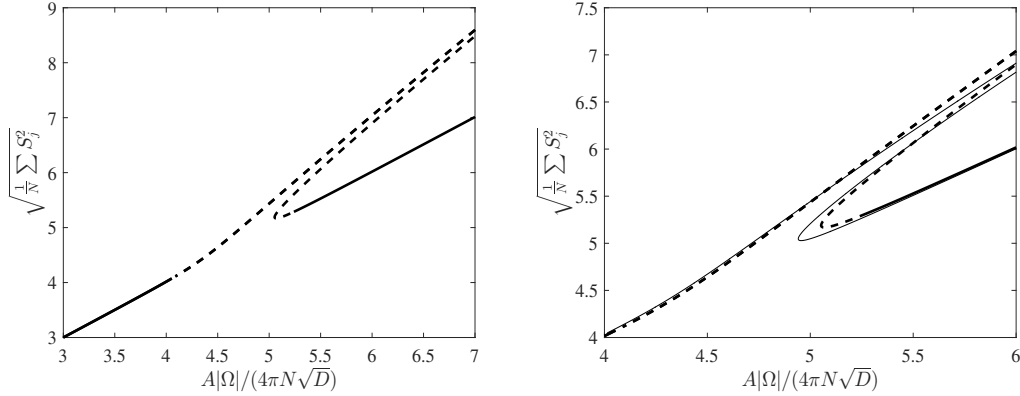


Figure 8. Left panel: bifurcation diagram of $\sqrt{N^{-1} \sum_i S_{i\varepsilon}^2}$ versus $A|\Omega|/(4\pi N\sqrt{D})$ computed from (2.34) using MATCONT [5] for $D = 0.1$ and $\varepsilon = 0.05$ when $N = 2$ spots are placed at $\mathbf{x}_1 = (0, 0, r_0 + 0.1)$ and $\mathbf{x}_2 = (0, 0, -r_0)$, with $r_0 = 0.429$, which corresponds to a small perturbation of the true equilibrium values as given in Table 1 and discussed in section 4. The dashed branches are the asymmetric solution branches. Since \mathbf{e} is not an eigenvector of \mathcal{G} , we observe an imperfection-sensitivity behavior for the quasi-equilibria. The numerical results for the saddle-node point are $S_1 \approx 5.72$ and $S_2 \approx 3.33$, which agree rather closely with the corresponding values $S_1 \approx 5.82$ and $S_2 \approx 3.23$ predicted from the $\varepsilon^{1/3}$ asymptotic theory. Right panel: favorable comparison of full numerical results (dotted and heavy solid lines) for the solution branches, computed from (2.34), with the asymptotic result (light solid line) from the cubic (2.44).

and we write S_1 and S_2 in terms of δ and some $\tilde{S} \ll 1$ as

$$(2.39) \quad S_1 = S_{cf} + \tilde{S} + \frac{\delta}{2}, \quad S_2 = S_{cf} + \tilde{S} - \frac{\delta}{2}.$$

Upon substituting (2.39) into (2.37), we obtain using Taylor series, together with $\mu'_0(S_{cf}) = 0$, that

$$(2.40) \quad -4\pi\varepsilon \left[S_{cf}(R_{11} - R_{22}) + \mathcal{O}(\tilde{S}, \delta) \right] = \mu''_0(S_{cf}) \left(\tilde{S}\delta + \mathcal{O}(\delta^2) \right) + \frac{\mu'''_0(S_{cf})}{3} \tilde{S}^3 + \mathcal{O}(\tilde{S}^2\delta, \tilde{S}\delta^2, \delta^3).$$

To balance the terms in (2.40) we need $\tilde{S} = \mathcal{O}(\varepsilon^{1/3})$ and $\tilde{S}\delta = \mathcal{O}(\varepsilon)$, which yields $\delta = \mathcal{O}(\varepsilon^{2/3})$. With this scaling, it readily follows that we can neglect the error terms written in (2.40). We then write $\tilde{S} = \varepsilon^{1/3}\tilde{S}_0$ and $\delta = \varepsilon^{1/3}\delta_0$, where \tilde{S}_0 satisfies the cubic

$$(2.41) \quad \frac{\mu'''_0(S_{cf})}{3} \tilde{S}_0^3 + \mu''_0(S_{cf}) \tilde{S}_0 \delta_0 = -4\pi S_{cf}(R_{11} - R_{22}).$$

From the numerical results used for Figure 3(a), we estimate that $\mu''_0(S_{cf}) \approx 0.15$ and $\mu'''_0(S_{cf}) \approx -0.12$. Relabeling the spots so that $R_{11} > R_{22}$ without loss of generality, we reduce (2.41) to a canonical cubic by introducing x and y by

$$(2.42a) \quad \tilde{S}_0 = \tilde{S}_{0d}y, \quad \delta_0 = \delta_{0d}x,$$

where \tilde{S}_{0d} and δ_{0d} are

$$(2.42b) \quad \tilde{S}_{0d} \equiv \left(\frac{12\pi S_{cf}(R_{11} - R_{22})}{|\mu'''_0(S_{cf})|} \right)^{1/3}, \quad \delta_{0d} \equiv \left(\frac{|\mu'''_0(S_{cf})|}{3} \right)^{1/3} \frac{[4\pi S_{cf}(R_{11} - R_{22})]^{2/3}}{\mu''_0(S_{cf})},$$

so that (2.41) reduces to the canonical cubic

$$(2.43) \quad y^3 - xy = 1.$$

This cubic always has one real solution $y_3 > 0$ for any x , and two additional real solutions y_1 and y_2 , with $y_1 < y_{\min} \equiv -2^{-1/3} < 0$ and $y_{\min} < y_2 < 0$, whenever $x > x_{\min} = 2^{-2/3} + 2^{1/3} \approx 1.8899$.

In summary, in terms of the roots of the cubic (2.43), and the scaling (2.42), the roots of (2.34) near S_{cf} are given in terms of x and y by

$$(2.44a) \quad \frac{A|\Omega|}{4\pi(2)\sqrt{D}} \sim S_{cf} + \left(\frac{\delta_{0d}}{2}\right) x\varepsilon^{2/3},$$

$$(2.44b) \quad S_1 \sim S_{cf} + \varepsilon^{1/3}\tilde{S}_{0d}y + \left(\frac{\delta_{0d}}{2}\right) x\varepsilon^{2/3}, \quad S_2 \sim S_{cf} - \varepsilon^{1/3}\tilde{S}_{0d}y + \left(\frac{\delta_{0d}}{2}\right) x\varepsilon^{2/3}.$$

The saddle-node bifurcation value associated with (2.44) is at

$$(2.45) \quad \left(\frac{A|\Omega|}{4\pi(2)\sqrt{D}}\right)_{sn} \sim S_{cf} + \left(\frac{\delta_{0d}}{2}\right) x_{\min}\varepsilon^{2/3}, \quad S_{cf} \approx 4.52, \quad x_{\min} \approx 1.8899.$$

For the unit ball, and for the specific two spot pattern of Figure 8 where $\varepsilon = 0.05$ and $D = 0.1$, (2.45) yields a value of 4.942, which is very close to the saddle-node point of 5.05 computed in the left panel of Figure 8. In the right panel of Figure 8 we show that the asymptotic result from the cubic (2.44) accurately predicts the imperfection-sensitive bifurcation structure of the full system (2.34) even when $\varepsilon = 0.05$. In Figure 9 we confirm the $\varepsilon^{2/3}$ prediction of (2.45) for the saddle-node location by comparing it on a log-log plot against full numerical results computed from (2.34) using MATCONT [5].

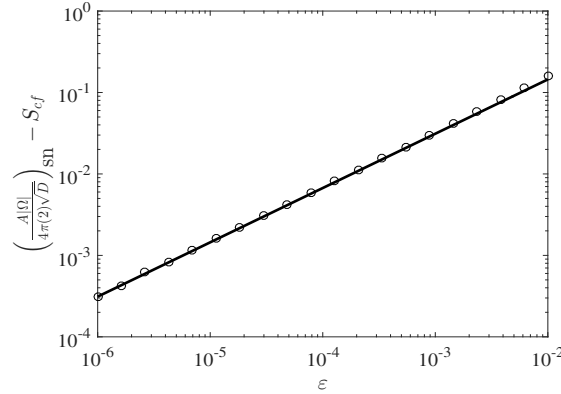


Figure 9. Log-log plot of $\left(\frac{A|\Omega|}{4\pi(2)\sqrt{D}}\right)_{sn} - S_{cf}$ versus ε characterizing the location of the saddle-node point on the asymmetric solution branch of Figure 8 versus ε . The solid curve corresponds to the asymptotic result (2.45), while the discrete points are computed from (2.34) using MATCONT [5]. This plot confirms the $\varepsilon^{2/3}$ scaling law of (2.45).

3. The linear stability of quasi-equilibrium patterns. In this section, we analyze the linear stability of symmetric quasi-equilibrium patterns. We begin by considering the effect of locally radially symmetric perturbations near each spot. We let v_{qe} and u_{qe} denote the N -spot symmetric quasi-equilibrium pattern, and in (1.2) we introduce the perturbation

$$(3.1) \quad v = v_{qe} + e^{\lambda t} \phi, \quad u = u_{qe} + e^{\lambda t} \psi, \quad \text{where } |\phi| \ll 1, \quad |\psi| \ll 1,$$

to obtain the linear eigenvalue problem

$$(3.2a) \quad \varepsilon^2 \Delta \phi - \phi + 2u_{qe}v_{qe}\phi + v_{qe}^2\psi = \lambda\phi, \quad \mathbf{x} \in \Omega, \quad \partial_n \phi = 0, \quad \mathbf{x} \in \partial\Omega,$$

$$(3.2b) \quad \frac{D}{\varepsilon} \Delta \psi - \frac{1}{\varepsilon^3} (2u_{qe}v_{qe}\phi + v_{qe}^2\psi) = \varepsilon^3 \lambda \psi, \quad \mathbf{x} \in \Omega, \quad \partial_n \psi = 0, \quad \mathbf{x} \in \partial\Omega.$$

In the inner region near the j th spot at $\mathbf{x} = \mathbf{x}_j$, we let

$$(3.3) \quad \phi \sim c_j \Phi_j(\rho), \quad \psi \sim \frac{c_j \Psi_j(\rho)}{D},$$

for some constant c_j to be determined. We then use the local behavior $v_{qe} \sim \sqrt{D}V_{j\varepsilon}(\rho)$ and $u_{qe} \sim U_{j\varepsilon}(\rho)/\sqrt{D}$ to obtain the leading-order inner eigenvalue problem

$$(3.4a) \quad \Delta_\rho \Phi_j - \Phi_j + 2V_{j\varepsilon}U_{j\varepsilon}\Phi_j + V_{j\varepsilon}^2\Psi_j = \lambda\Phi_j, \quad 0 < \rho < \infty; \quad \Phi_j'(0) = 0, \quad \Phi_j \rightarrow 0, \quad \text{as } \rho \rightarrow \infty,$$

$$(3.4b) \quad \Delta_\rho \Psi_j - 2V_{j\varepsilon}U_{j\varepsilon}\Phi_j - V_{j\varepsilon}^2\Psi_j = 0, \quad 0 < \rho < \infty; \quad \Psi_j'(0) = 0.$$

We will impose the normalization condition that $\lim_{\rho \rightarrow \infty} \rho^2 \partial_\rho \Psi_j = -1$, so that we have the following far-field behavior in terms of some function $B_j = B_j(\lambda; S_{j\varepsilon})$:

$$(3.4c) \quad \Psi_j \sim \frac{1}{\rho} + B_j(\lambda; S_{j\varepsilon}), \quad \text{as } \rho \rightarrow \infty.$$

Here $S_{j\varepsilon}$, for $j = 1, \dots, N$, is to be determined from the nonlinear algebraic system (2.34). By applying the divergence theorem to (3.4b), we obtain the integral identity

$$(3.5) \quad \int_0^\infty (2V_{j\varepsilon}U_{j\varepsilon}\Phi_j + V_{j\varepsilon}^2\Psi_j) \rho^2 d\rho = -1.$$

Now in the outer region, the reaction term in (3.2b) of order $\mathcal{O}(\varepsilon^{-3})$ is localized. Therefore, in the sense of distributions we write

$$\varepsilon^{-3} (2u_{qe}v_{qe}\phi + v_{qe}^2\psi) \rightarrow 4\pi \sum_{j=1}^N c_j \left[\int_0^\infty (2V_{j\varepsilon}U_{j\varepsilon}\Phi_j + V_{j\varepsilon}^2\Psi_j) \rho^2 d\rho \right] \delta(\mathbf{x} - \mathbf{x}_j) = -4\pi \sum_{j=1}^N c_j \delta(\mathbf{x} - \mathbf{x}_j),$$

so that the outer equation for ψ is

$$(3.6) \quad \Delta \psi = -\frac{4\pi\varepsilon}{D} \sum_{i=1}^N c_i \delta(\mathbf{x} - \mathbf{x}_i), \quad \mathbf{x} \in \Omega; \quad \partial_n \psi = 0, \quad \mathbf{x} \in \partial\Omega.$$

The exact solution to (3.6) is

$$(3.7) \quad \psi = \bar{\psi} + \frac{4\pi\varepsilon}{D} \sum_{i=1}^N c_i G(\mathbf{x}; \mathbf{x}_i),$$

where $\bar{\psi}$ is a constant to be determined, and $G(\mathbf{x}; \mathbf{x}_i)$ is the Neumann Green's function satisfying (2.10). Then by applying the divergence theorem to (3.6) we obtain the solvability condition

$$(3.8) \quad \sum_{j=1}^N c_j = 0.$$

In view of (3.1) and (3.8) we see that the perturbation preserves the sum of the spot amplitudes. As such, this type of instability is referred to as a competition instability (cf. [17]).

Next, we derive a linear algebraic system for the constants c_j , $j = 1, \dots, N$, and $\bar{\psi}$. We expand (3.7) as $\mathbf{x} \rightarrow \mathbf{x}_j$ and, in terms of inner variables, we get

$$(3.9) \quad \psi \sim \bar{\psi} + \frac{c_j}{D\rho} + \frac{4\pi\varepsilon}{D} (\mathcal{G}\mathbf{c})_j, \quad \text{as } \mathbf{x} \rightarrow \mathbf{x}_j,$$

where $\rho \equiv \varepsilon^{-1}|\mathbf{x} - \mathbf{x}_j|$, \mathcal{G} is the Neumann Green's matrix, and $\mathbf{c} \equiv (c_1, \dots, c_N)^T$. This local behavior of the outer eigenfunction must match the far-field behavior of the corresponding inner solution, given by $\psi \sim c_j D^{-1} (B_j + 1/\rho)$ as $\rho \rightarrow \infty$. In this way, we obtain that \mathbf{c} and $\bar{\psi}$ satisfy

$$(3.10) \quad c_j B_j = D\bar{\psi} + 4\pi\varepsilon (\mathcal{G}\mathbf{c})_j, \quad j = 1, \dots, N; \quad \sum_{i=1}^N c_i = 0,$$

where $B_j = B_j(\lambda; S_j\varepsilon)$. By eliminating $\bar{\psi}$, we readily derive in matrix form that \mathbf{c} satisfies the matrix eigenvalue problem

$$(3.11) \quad (I - \mathcal{E})(\mathcal{B} - 4\pi\varepsilon\mathcal{G})\mathbf{c} = 0, \quad \mathcal{E} \equiv \frac{1}{N}\mathbf{e}\mathbf{e}^T; \quad \mathbf{e}^T\mathbf{c} = 0,$$

where $\mathbf{e} = (1, \dots, 1)^T$, and where \mathcal{B} is the diagonal matrix with entries $(\mathcal{B})_{jj} = B_j$ and $(\mathcal{B})_{ij} = 0$ for $i, j = 1, \dots, N$. The discrete eigenvalues λ of the linearization (3.2) are roots of $\det((I - \mathcal{E})(\mathcal{B} - 4\pi\varepsilon\mathcal{G})) = 0$, provided that the corresponding eigenvector \mathbf{c} satisfies the side constraint $\mathbf{e}^T\mathbf{c} = 0$.

We first consider the leading-order theory associated with (3.11). To leading order in ε , we obtain that $S_j = S_c + \mathcal{O}(\varepsilon)$ for $j = 1, \dots, N$, where S_c is defined in (2.14), and $U_{j\varepsilon} \sim U_c + \mathcal{O}(\varepsilon)$ and $V_{j\varepsilon} \sim V_c + \mathcal{O}(\varepsilon)$, where U_c and V_c satisfy the core problem (2.16). As a result, we obtain that $\mathcal{B} = B(\lambda; S_c)I + \mathcal{O}(\varepsilon)$, where $B(\lambda; S_c)$ is to be computed from the following common core problem that is the same for each spot:

(3.12a)

$$\Delta_\rho \Phi_c - \Phi_c + 2V_c U_c \Phi_c + V_c^2 \Psi_c = \lambda \Phi_c, \quad 0 < \rho < \infty; \quad \Phi_c'(0) = 0, \quad \Phi_c \rightarrow 0, \quad \text{as } \rho \rightarrow \infty,$$

$$(3.12b) \quad \Delta_\rho \Psi_c - 2V_c U_c \Phi_c - V_c^2 \Psi_c = 0, \quad 0 < \rho < \infty; \quad \Psi_c'(0) = 0, \quad \Psi_c \sim \frac{1}{\rho} + B(\lambda; S_c), \quad \text{as } \rho \rightarrow \infty.$$

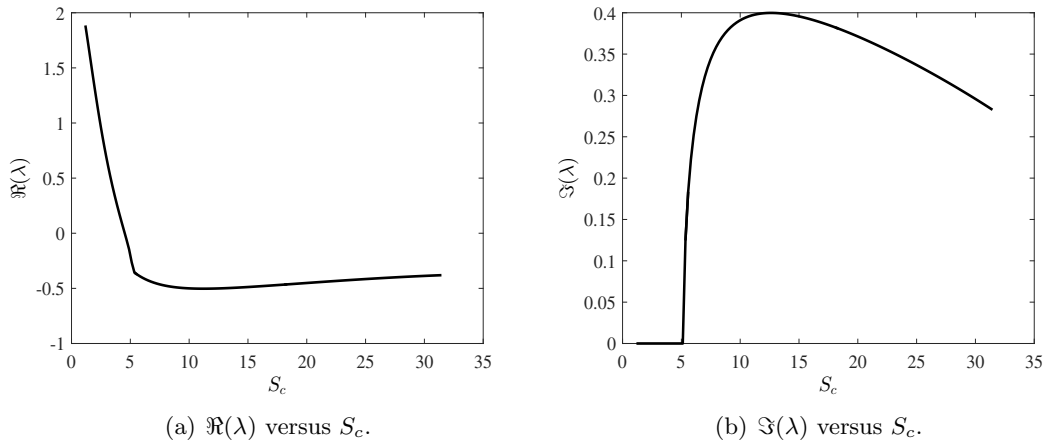


Figure 10. The real (a) and imaginary (b) parts of the eigenvalue with largest real part corresponding to the leading-order competition instability criterion (3.13). As S_c decreases, there is a complex conjugate pair of eigenvalues that collide on the negative real axis when $S_c \approx 5.12$. As S_c is decreased further, a real eigenvalue crosses into the right half-plane when $S_c = S_{cf} \approx 4.52$.

For $N \geq 2$, the leading-order term in (3.11) yields that the discrete eigenvalues λ of the linearization (3.2) satisfy

$$(3.13) \quad B(\lambda; S_c) = 0,$$

and that for $N \geq 2$ the allowable amplitude perturbations \mathbf{c} consists of the $(N-1)$ -dimensional subspace where $\mathbf{e}^T \mathbf{c} = 0$.

We first suppose that λ is real-valued, and we solve (3.12) numerically, subject to the side constraint (3.13). In Figure 10 we plot the real and imaginary parts of the corresponding eigenvalue with largest real part as a function of S_c . For S_c sufficiently large (not shown), our computations of the root of (3.13) with the largest real part shows that λ is negative real. As S_c decreases, two real negative eigenvalues collide and split, forming a complex conjugate pair in the left half-plane. As S_c decreases further, as shown in Figure 10, this pair hits the negative real axis when $S \approx 5.12$ and $\lambda \approx -0.2$. One of the eigenvalues remains in the left half-plane on the negative real axis, while the other eigenvalue crosses into the unstable right half-plane along the real axis, triggering a competition instability as a result of a zero-eigenvalue crossing. We claim that the value $S_c = S_{\text{comp}}$ at which this crossing occurs corresponds precisely with the minimum point of the graph $\mu_0(S_c)$ versus S_c shown in Figure 3(a). To see this, we observe upon differentiating the core problem (2.16) with respect to S_c that the resulting problem is precisely the inner eigenvalue problem (3.12) with $\lambda = 0$, which gives rise to the equivalence $B(0; S_c) = -\mu'_0(S_c)$. With the required condition $B(\lambda; S_c) = 0$, we conclude that the leading-order competition threshold must occur at $S_{\text{comp}} = S_{cf} \approx 4.52$.

Next, we consider the possibility that an instability arises through a Hopf bifurcation, whereby a complex conjugate pair of eigenvalues enters $\Re(\lambda) > 0$ through the imaginary axis. We let $\lambda = i\lambda_I$ in (3.12) and, upon separating the resulting system into real and imaginary parts, we readily compute the modulus $|B(i\lambda_I; S_c)|$ numerically as a function of

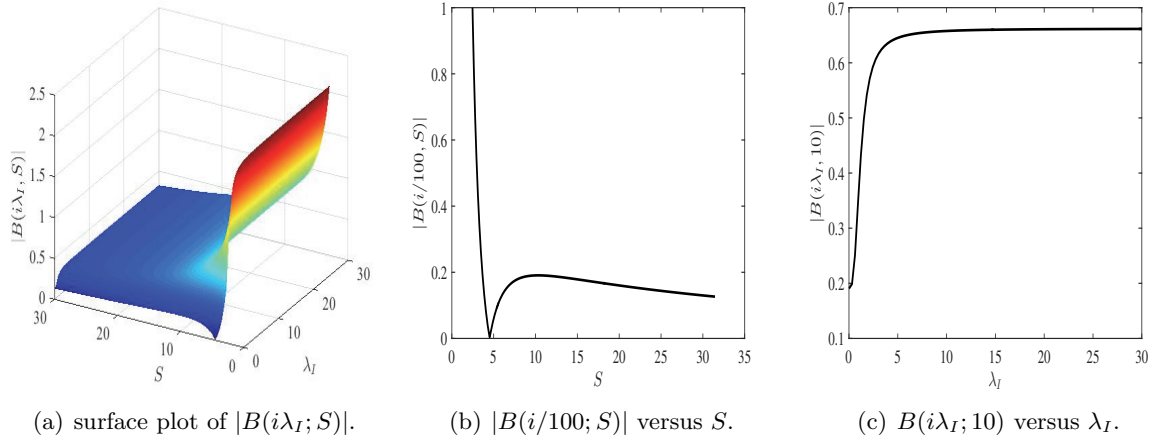


Figure 11. In (a), we plot the numerically computed surface $|B(i\lambda_I; S)|$ for $0 < S < 30$ and $0 < \lambda_I < 30$, showing that $|B(i\lambda_I; S)| > 0$ holds. In (b) we plot the slice $|B(i/100; S)|$ versus S , showing, as expected, that $|B(i/100; S)|$ is very small when $S = S_{cf} \approx 4.52$. In (c), we plot the slice $|B(i\lambda_I; 10)|$ versus λ_I .

S_c and $\lambda_I > 0$. The surface plot and slices through the surface shown in Figure 11 verify that the strict inequality $|B(i\lambda_I; S_c)| > 0$ holds, and so there can be no Hopf bifurcation as S_c is varied. Since for $S_c \ll 1$, (3.12) is readily seen to reduce to leading order to the scalar self-adjoint local eigenvalue problem $\mathcal{L}\Phi_{c0} = \lambda\Phi_{c0}$, where \mathcal{L} is defined in (2.20), which has no imaginary eigenvalues, it follows by continuity of the eigenvalue path with respect to S_c that any complex-valued eigenvalues for (3.12), with the side constraint (3.13), must remain in the stable left half-plane $\Re(\lambda) < 0$ for any $S_c > 0$.

Overall, the numerical results of Figures 10 and 11 show that to leading order in ε , the N -spot quasi-equilibrium pattern is linearly stable (unstable) to a competition instability when $S_c > S_{\text{comp}}$ ($S_c < S_{\text{comp}}$). In terms of the parameters A and D , we obtain from (2.14) that to leading order in ε , a quasi-equilibrium pattern of N identical spots is linearly stable to a competition instability when

$$(3.14) \quad \frac{A|\Omega|}{4\pi N\sqrt{D}} > S_{\text{comp}} = S_{cf} \approx 4.52.$$

That is, a competition instability is triggered when the total inhibitor feed-rate $A|\Omega|$ is insufficient to sustain the N spots, or when the interaction of the spots, mediated by the diffusion coefficient D of the inhibitor, is sufficiently strong.

We now make several remarks. First, the leading-order-in- ε linear stability criterion (3.14) is independent of where the spots are located. Second, with the competition threshold coinciding with the minimum point of the graph $\mu_0(S_c)$, the entire left (right) branch of $\mu_0(S_c)$ is unstable (linearly stable) to a competition instability. Finally, while this leading-order analysis determines when a symmetric quasi-equilibrium pattern loses stability when $N \geq 2$, it gives no information regarding which mode of instability is most dominant. This is unsurprising, since all spots are identical to leading order, regardless of location. A higher-order analysis is thus required to determine the dominant mode. We will provide such a higher-order theory

below when the spot configuration has a special structure.

In Figure 12, we illustrate our leading-order theory by solving (1.2) for an initial configuration of two antipodal spots located at $(0, \pm 0.429, 0)$ inside a unit ball (see Figure 13 for the initial configuration). In Figure 12(a), we set the parameters $D = 0.092$ and $A = 10$ so that $S_c \approx 5.5$. We initialize the spots so that the amplitude of one is slightly larger than that of the other. Since $S_c > S_{\text{comp}}$, we observe no competition instability. In particular, since $S_c > 5.12$, for which there is a complex conjugate eigenvalue pair in the left half-plane (see Figure 10), we observe in Figure 12 that the spot amplitudes oscillate out of phase in a manner consistent with $\mathbf{c}^T \mathbf{e} = 0$ as they settle to their steady-state value. In Figure 12(b), we set $D = 0.143$ and $A = 10$ so that $S_c \approx 4.4$. Since $S_c < S_{\text{comp}}$, we observe that the linear competition instability triggers a nonlinear event leading to the collapse on an $\mathcal{O}(1)$ time-scale of only one of the two spots.

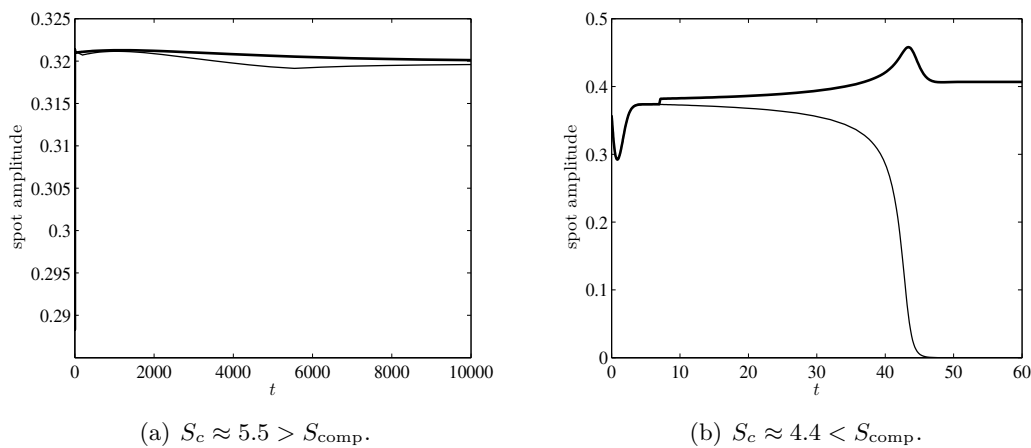


Figure 12. Plots of the amplitude of two antipodal spots located at $(0, \pm 0.429, 0)$ as computed from numerically solving (1.2) using FlexPDE6 [6]. In (a), we set $D = 0.092$ and $A = 10$ so that $S_c \approx 5.5 > S_{\text{comp}} \approx 4.52$. The amplitudes appear to oscillate out of phase as they settle to their steady-state values. In (b), $D = 0.143$ and $A = 10$ so that $S_c \approx 4.4 < S_{\text{comp}}$. The linear competition instability is seen to trigger a nonlinear event leading to the collapse of one of the two spots. In (a), $\varepsilon = 0.02$, while in (b), $\varepsilon = 0.01$.

For the case $N = 1$ of a one spot solution, the solvability condition (3.8) would require that $c_1 = 0$ unless the integral in (3.5) were identically zero. To have $c_1 \neq 0$, the far-field condition in (3.12b) must, therefore, be replaced with the condition that $\Psi \rightarrow 1$ as $\rho \rightarrow \infty$. That is, Ψ must be a constant at infinity. From a numerical solution of (3.12) with this modified far-field behavior, we show in Figure 14 that the eigenvalue with largest real part always lies in the left half-plane. Therefore, the one spot solution is always linearly stable to a radially symmetric perturbation.

Next, for $N \geq 2$, we extend the leading-order stability theory to capture the weak effects on the stability thresholds of the locations of the spots for the special case where the spots are aligned so that \mathbf{e} is an eigenvector of the Green's matrix \mathcal{G} . In the unit ball such patterns occur when spots are located at vertices of a platonic solid concentric within the ball, when spots are equally spaced along an equator concentric within the ball, and for some of the equilibrium

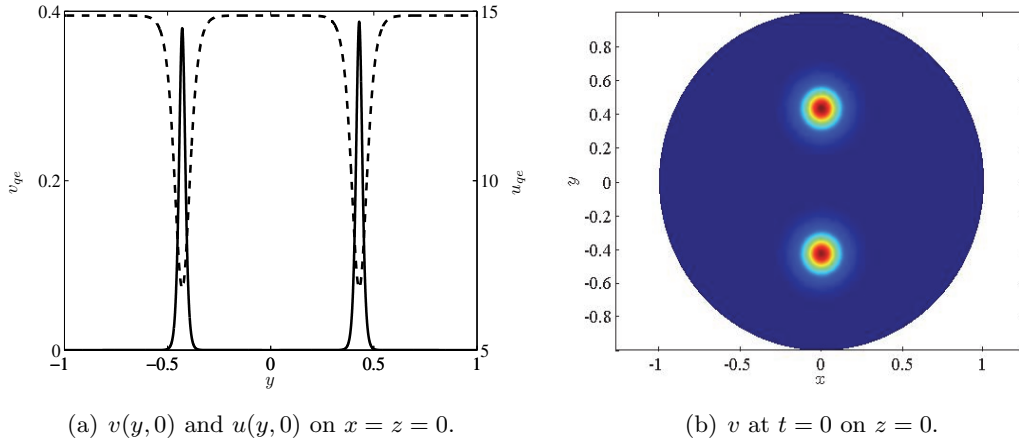


Figure 13. Typical initial conditions for numerical solutions of (1.2) on the unit ball. Two antipodal spots are located at $(0, \pm 0.429, 0)$. In (a), we plot v (solid line) and u (dashed line) at $t = 0$ as a function of y on the line $x = z = 0$. In (b), we show a surface plot of v on the plane $z = 0$. Here, $D = 0.143$, $A = 10$, and $\varepsilon = 0.01$. The surface plot (b) has been slightly altered for clarity.

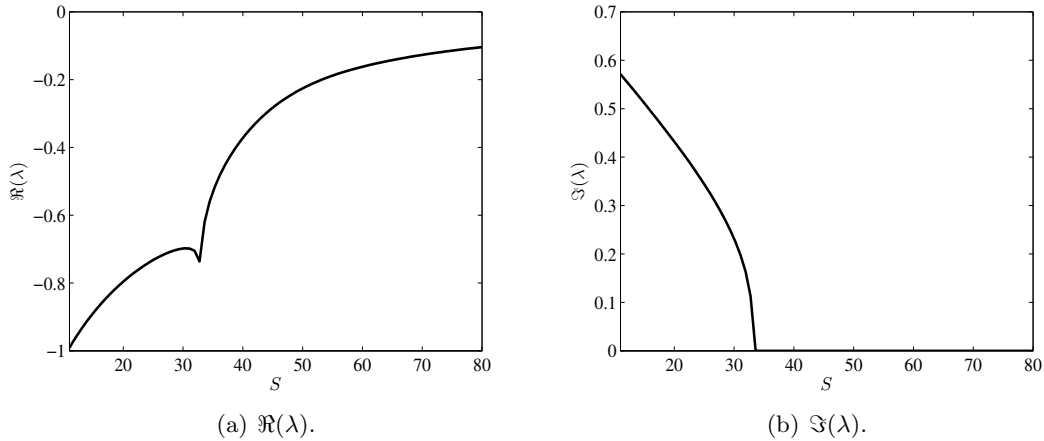


Figure 14. The real (a) and imaginary (b) parts of the eigenvalue with largest real part corresponding to a radially symmetric perturbation of a one spot solution. The real part is negative for all S . For $S \lesssim 10$ (not shown), the largest eigenvalue becomes -1 due to discretization and is therefore absorbed into the continuous spectrum located on the negative real axis with $\lambda \leq -1$.

configurations of the spot dynamics (4.13) derived in section 4. For such patterns, it follows from the fact that \mathcal{G} is symmetric that its matrix spectrum is

$$(3.15) \quad \mathcal{G}\mathbf{e} = k_1\mathbf{e}; \quad \mathcal{G}\mathbf{q}_j = k_j\mathbf{q}_j, \quad \mathbf{q}_j^T \mathbf{e} = 0, \quad j = 2, \dots, N, \quad \mathbf{q}_j^T \mathbf{q}_i = 0, \quad i \neq j.$$

We recall from the discussion following (2.36) that when $\mathcal{G}\mathbf{e} = k_1\mathbf{e}$, there is a common source strength solution to (2.34) that is the same as that for the leading-order solution in (2.14), i.e., that $S_{j\varepsilon} = S_c$ for all $j = 1, \dots, N$, where S_c is defined in (2.14). In addition, we

have $U_{j\varepsilon} = U_c + \mathcal{O}(\varepsilon^2)$ and $V_{j\varepsilon} = V_c + \mathcal{O}(\varepsilon^2)$, so that $\mathcal{B} = B(\lambda; S_c)I + \mathcal{O}(\varepsilon^2)$ in (3.11). As a result, with a negligible error of $\mathcal{O}(\varepsilon^2)$, we obtain for $N \geq 2$ from (3.11) that

$$(3.16) \quad B(\lambda; S_c) = 4\pi\varepsilon k_j, \quad \text{when } \mathbf{c} = \mathbf{q}_j, \quad j = 2, \dots, N.$$

To determine the critical values for S_c at the stability threshold, we set $\lambda = 0$ in (3.16) and use $B(0; S_c) = -\mu'_0(S_c)$, which yields the $N - 1$ nonlinear algebraic equations

$$(3.17) \quad \mu'_0(S_c) = -4\pi\varepsilon k_j, \quad j = 2, \dots, N.$$

To determine the root of (3.17) for each j , we expand $S_c = S_{cf} + \varepsilon\tilde{S}_j$, and by using $\mu'_0(S_{cf}) = 0$, we readily calculate

$$(3.18) \quad \tilde{S}_j = -\frac{4\pi k_j}{\mu''_0(S_{cf})}, \quad j = 2, \dots, N.$$

We conclude that there are zero-eigenvalue crossings whenever $S_c = S_{cf} + \varepsilon\tilde{S}_j + \dots$ for $j = 2, \dots, N$. The competition instability threshold will then correspond to the largest of these possible values for \tilde{S}_j . Since $\mu''_0(S_{cf}) > 0$ from Figure 3(a), this threshold will be determined by the smallest of the eigenvalues of \mathcal{G} in the subspace perpendicular to \mathbf{e} . We summarize this result as follows.

Main Result 3.1. *Let $\varepsilon \rightarrow 0$ and $N \geq 2$, and suppose that the spots are aligned so that $\mathbf{e} = (1, \dots, 1)^T$ is an eigenvector of the Neumann Green's matrix \mathcal{G} . Then, the N -spot quasi-equilibrium solution is linearly stable to a competition instability on an $\mathcal{O}(1)$ time-scale if and only if*

$$(3.19) \quad S_c > S_{\text{comp}} \equiv S_{cf} - \frac{4\pi\varepsilon}{\mu''_0(S_c)} \min_{j=2, \dots, N} k_j, \quad \text{where } S_c \equiv \frac{A|\Omega|}{4\pi N\sqrt{D}}.$$

Here k_j for $j = 2, \dots, N$ are the eigenvalues of \mathcal{G} in the subspace perpendicular to \mathbf{e} (see (3.15)). In addition, $S_{cf} \approx 4.52$ is the minimum point of the graph of $\mu_0(S_c)$ versus S_c shown in Figure 3(a), where we estimate that $\mu''_0(S_{cf}) \approx 0.15$. Equivalently, we predict that such a pattern is linearly stable on an $\mathcal{O}(1)$ time-scale if and only

$$(3.20) \quad D < D_{\text{comp}} \equiv \frac{(A|\Omega|)^2}{16\pi^2 N^2} \left(S_{cf} - \frac{4\pi\varepsilon}{\mu''_0(S_c)} \min_{j=2, \dots, N} k_j \right)^{-2}.$$

For the unit ball, we now compare the prediction of (3.19) and (3.20) with full numerical results computed from FlexPDE6 [6] for a symmetric two spot pattern with spots at $\mathbf{x}_1 = (0, 0, r_0)$ and $\mathbf{x}_2 = -\mathbf{x}_1$, and for the four-spot tetrahedral pattern of Figure 7(a) of section 2.1. A pattern was classified as unstable when the amplitude of one of the spots collapsed to zero on an $\mathcal{O}(1)$ time-scale (as in Figure 12(b)) while deemed not to be caused by a triggering due to slow spot dynamics (see brief discussion below). Otherwise, the pattern was classified as stable. The results of these computations for $\varepsilon = 0.03$, $A = 10$ are shown in Figure 15(a),(b), where numerically stable (unstable) parameter sets are marked by solid (open) circles. The leading-order competition stability threshold is indicated by the dashed line, while the refined

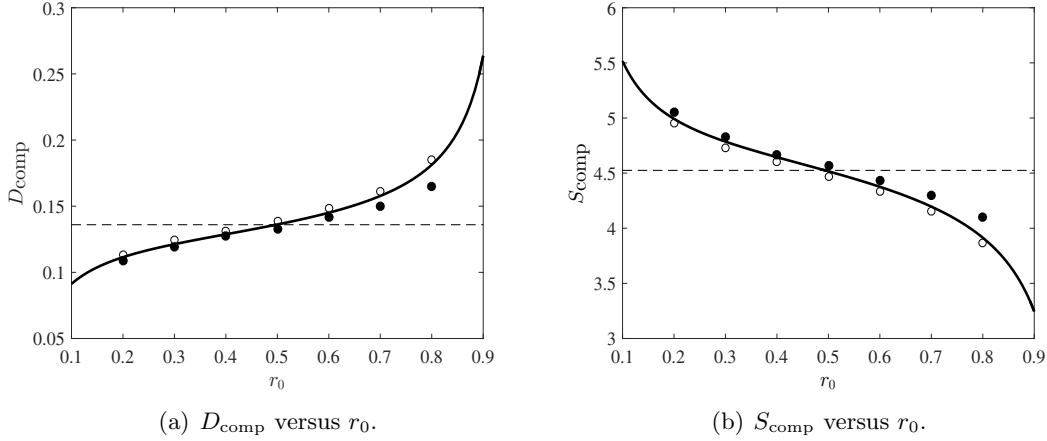


Figure 15. Comparison of the predictions of the refined competition stability threshold (3.19) (solid curves) with the full numerical results computed from (1.2) using FlexPDE6 [6] for a two spot pattern with spots at $\mathbf{x}_1 = (0, 0, r_0)$ and $\mathbf{x}_2 = -\mathbf{x}_1$ for $A = 10$ and $\varepsilon = 0.03$ inside the unit ball. The vertical axis is D_{comp} (a) and S_{comp} (b). The solid (open) dots represent parameter sets where the pattern was observed numerically from FlexPDE6 to be stable (unstable). The horizontal dotted lines are the leading-order competition thresholds $D_{\text{comp}} \equiv (A^2 S_{cf}^{-2})/36 \approx 0.136$ (a) and $S_{\text{comp}} \equiv S_{cf} \approx 4.52$ (b).

threshold is plotted in the heavy solid line. As expected, the smaller the distance between the spots, the smaller the diffusivity D must be in order for the pattern to be stable. We observe excellent agreement between the refined asymptotic theory and results from the full PDE solution.

Similarly, in Figure 16(a),(b) with $\varepsilon = 0.03$ and $D = 1$, we show a favorable comparison between the refined stability threshold (3.19) and full numerical results computed from (1.2) using FlexPDE6 [6] for the case where $N = 4$ spots are placed at the vertices of a tetrahedron of radius $r_0 < 1$ concentric within the unit ball. The true steady-state of the slow dynamics is when $r_0 = 0.564$ (see Table 1). For this case, there is a mode degeneracy in that $k_2 = k_3 = k_4$, so that up to $\mathcal{O}(\varepsilon)$ terms the entire 3-D subspace perpendicular to \mathbf{e} becomes unstable as S_c crosses below S_{comp} . As a result, although the refined stability theory determines the stability threshold, the linearized stability theory is not capable of identifying which mode of instability is dominant.

We make three remarks. First, with regards to numerically determining the stability of quasi-equilibrium patterns, the process was made difficult by the slow drift of concentric patterns to their equilibrium radius r_c (see Table 1 of section 4). When $r_0 > r_c$, an originally stable pattern may become unstable as the spots drift closer together. Starting close to threshold, the dynamics can destabilize a pattern rather quickly when ε is only moderately small. Thus, a pattern needed to be initialized farther below threshold in order to be more assuredly classified as stable, resulting in apparently poorer agreement with asymptotics when $r_0 > r_c$. When $r_0 < r_c$, dynamics increases distances between spots so that an originally stable pattern will remain stable for all time. On the other hand, the $\mathcal{O}(1)$ instability of an unstable pattern will trigger before the $\mathcal{O}(\varepsilon^3)$ dynamics can stabilize it. This results in seemingly

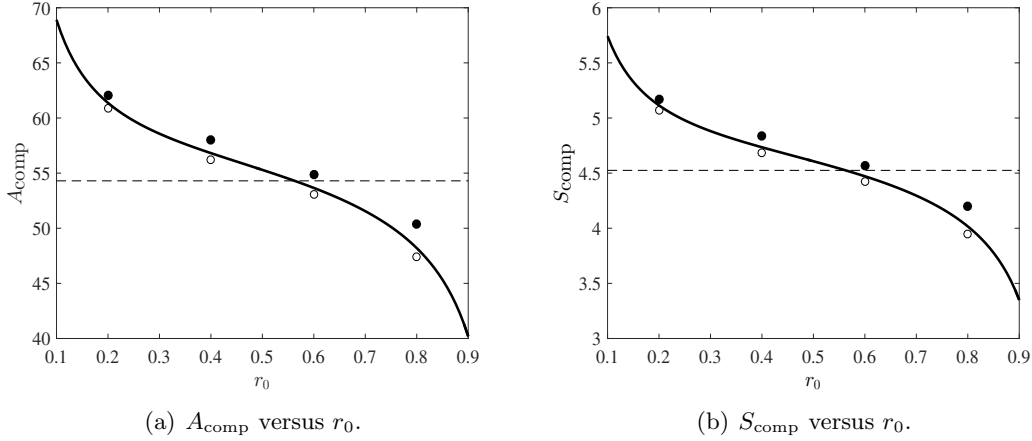


Figure 16. Comparison of the predictions of the refined competition stability threshold (3.19) (solid curves) with the full numerical results computed from (1.2) using FlexPDE6 [6] for a four-spot pattern with spots centered at the vertices of a tetrahedron of radius $r_0 < 1$ concentric within the unit ball. The parameters are $D = 1$ and $\varepsilon = 0.03$. The vertical axis is the competition instability threshold for A (a) and S (b). The solid (open) dots represent parameter sets where the pattern was observed numerically from FlexPDE6 to be stable (unstable). The horizontal dotted lines are the leading-order competition thresholds $A_{\text{comp}} \equiv 12\sqrt{D}S_{cf} \approx 54.24$ (a) and $S_{\text{comp}} = S_{cf} \approx 4.52$ (b).

better agreement with asymptotics when $r_0 < r_c$. Second, even though the linear theory predicts that all modes destabilize simultaneously at $S = S_{\text{comp}}$, we have only numerically observed the annihilation of a single spot at a time, regardless of initial conditions. This mode selection may be due to an effect of higher order than the above analysis can capture. Finally, for the case where \mathbf{e} is not an eigenvector of \mathcal{G} , it is much more challenging to calculate ε -dependent correction terms to the leading-order competition stability threshold S_{cf} , and we do not perform this analysis here. This difficulty arises due to the need to resolve the intricate imperfection-sensitive bifurcation structure that exists near S_{cf} whenever \mathbf{e} is not an eigenvector of \mathcal{G} .

3.1. Linear stability of asymmetric patterns. In this subsection we briefly formulate the leading-order linear stability problem for the asymmetric patterns of (2.21). It is beyond the scope of this paper to give a comprehensive study of the stability of these patterns, and we give only a partial result showing the instability of asymmetric patterns for which $N_r \geq N_\ell$. While previous studies of 2-D spot problems (cf. [25], [18]) have found that certain asymmetric patterns can be stable in a particular regime, we have not been able to numerically observe any stable asymmetric patterns (even when $N_r < N_\ell$) in the 3-D Schnakenberg model, perhaps owing to the small domain of attraction of such patterns.

The formulation of the linear stability problem proceeds in a manner similar to that for the symmetric pattern, with the critical difference being that $B(\lambda; S)$ need not be zero. The relationship $B(\lambda; S)$ must therefore be determined in order to determine stability. To begin, we index the spots so that spots corresponding to strength $S_{\ell,r}$ are located at $\mathbf{x}_j^{(\ell,r)}$, for $j = 1, \dots, N_{\ell,r}$. Then in the inner region near $\mathbf{x}_j^{(\ell,r)}$ where $(v_{qe}, u_{qe}) \sim (\sqrt{D}\nu^{(\ell,r)}, \mu^{(\ell,r)}/\sqrt{D})$,

we let $\phi \sim c_j^{(\ell,r)} \Phi^{(\ell,r)}(\rho)$ and $\psi \sim c_j^{(\ell,r)} \Psi^{(\ell,r)}(\rho)/D$ in (3.2). This results in the inner eigenvalue problem of (3.4) with the far-field condition $\Psi^{(\ell,r)} \sim 1/\rho + B(\lambda; S_{\ell,r})$. By the same matching procedure leading to (3.10), we have that

$$(3.21) \quad \frac{c_j^{(\ell)} B(\lambda; S_\ell)}{D} = \psi_0, \quad \frac{c_j^{(r)} B(\lambda; S_r)}{D} = \psi_0.$$

The weights associated with the perturbation of each type of spot must then have a common value, so that

$$(3.22) \quad c_j^{(\ell)} = c_\ell, \quad j = 1, \dots, N_\ell; \quad c_j^{(r)} = c_r, \quad j = 1, \dots, N_r.$$

Together with (3.21), (3.22) yields the first equation for c_ℓ and c_r ,

$$(3.23a) \quad B(\lambda; S_\ell) c_\ell - B(\lambda; S_r) c_r = 0,$$

while the second equation comes from the solvability condition (3.8), which we rewrite as

$$(3.23b) \quad N_\ell c_\ell + N_r c_r = 0.$$

A nontrivial solution to the system (3.23) exists if and only if λ satisfies the transcendental equation $\mathcal{K}(\lambda) = 0$, where

$$(3.24) \quad \mathcal{K}(\lambda) \equiv \frac{N_r}{N_\ell} + \frac{B(\lambda; S_r)}{B(\lambda; S_\ell)},$$

where for given positive integers N_r and N_ℓ , the source strengths S_ℓ and S_r are determined by the nonlinear algebraic system (2.22). The asymmetric pattern is unstable if (3.24) has a root in $\Re(\lambda) > 0$, and it is linearly stable if all roots to (3.24) are in $\Re(\lambda) < 0$.

We now give a numerically assisted proof for the existence of at least one positive real root of (3.24) when $N_r \geq N_\ell$. We first recall that $B(0, S) = -\mu'_0(S)$. Together with the one-sided inverse functions $S_\ell = S_\ell(\mu_0)$ and $S_r = S_r(\mu_0)$ of the map $\mu_0(S)$, we obtain

$$(3.25) \quad \mathcal{K}(0) \equiv \frac{N_r}{N_\ell} - \mathcal{D}(\mu_0); \quad \mathcal{D}(\mu_0) \equiv -\frac{\mu'_0[S_r(\mu_0)]}{\mu'_0[S_\ell(\mu_0)]} > 0.$$

The function $\mu_0(S)$ is shown in Figure 3(a). Observe that $\mu'_0(S) > 0$ ($\mu'_0(S) < 0$) when $S > S_{cf}$ ($S < S_{cf}$). In Figure 17(a) we plot the numerically computed function $\mathcal{D}(\mu_0)$ versus μ_0 on $\mu_0 > \mu_{0\min}$, where $\mu_{0\min} = \mu_0(S_{cf})$. By L'Hopital's rule we must have $\mathcal{D}(\mu_{0\min}) = 1$. However, our plot in Figure 17(a) shows that $0 < \mathcal{D}(\mu_0) < 1$ for $\mu_0 > \mu_{0\min}$. Therefore, when $N_r \geq N_\ell$, we have from (3.25) that $\mathcal{K}(0) > 0$. Next, we note that because the entire right branch of $\mu_0(S)$ is stable with respect to positive real eigenvalues, $B(\lambda; S_r)$ must be of only one sign when λ is positive real. With $B(0; S_r) = -\mu'_0[S_r(\mu_0)] < 0$, we have that $B(\lambda; S_r) < 0$ for all $\lambda > 0$. Now since the left branch is unstable to a competition instability, there must exist a λ_c positive real such that $B(\lambda_c; S_\ell) = 0$. With $B(0; S_\ell) = -\mu'_0[S_\ell(\mu_0)] > 0$, we must have $B(\lambda; S_\ell) > 0$ when $0 < \lambda < \lambda_c$. Therefore, as $\lambda \rightarrow \lambda_c^-$, $\mathcal{K} \rightarrow -\infty$. Using that $\mathcal{K}(0) > 0$ whenever $N_r \geq N_\ell$, we conclude from the intermediate value theorem that there must exist

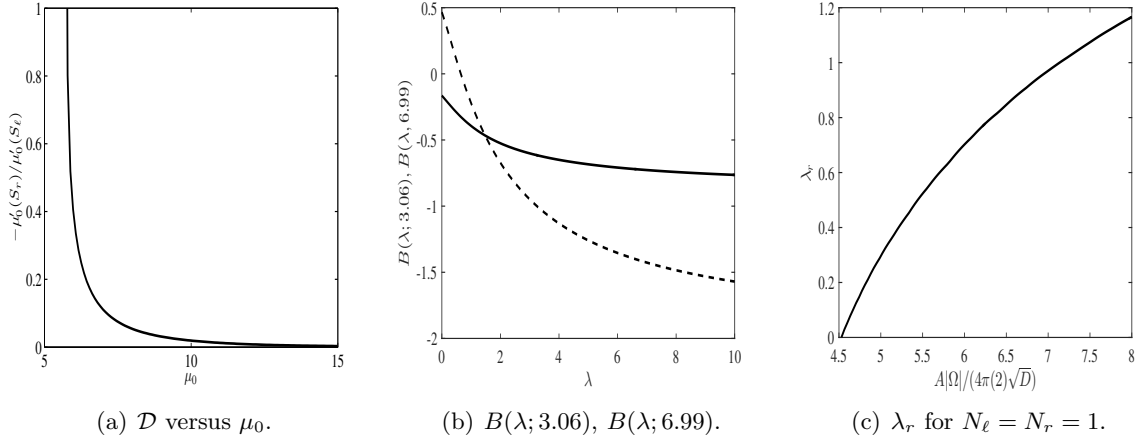


Figure 17. In (a), we plot $\mathcal{D}(\mu_0)$ defined in (3.25) versus μ_0 on $\mu_0 > \mu_{0min}$. Here, $S_\ell < S_{cf}$ ($S_r > S_{cf}$) is the smaller (larger) value of S associated with $\mu_0(S)$ (see Figure 3(a)). In (b), we plot $B(\lambda; S_\ell)$ (dashed line) and $B(\lambda; S_r)$. Here, $S_\ell = 3.06$ and $S_r = 6.99$ are solutions of (2.22) with $N_\ell = N_r = 1$ and $A|\Omega|/(4\pi\sqrt{D}) = 10.05$. For the particular parameters used, $B(\lambda; S_\ell)$ crosses 0 at $\lambda_c \approx 0.65$, while $B(\lambda; S_r)$ has constant sign. In (c), with $N_\ell = N_r = 1$, we plot the positive root of $\mathcal{K}(\lambda)$ in (3.24) satisfying $0 < \lambda_r < \lambda_c$. Observe that $\lambda_r \rightarrow 0^+$ as $A|\Omega|/(4\pi(2)\sqrt{D}) \rightarrow S_{cf}^+$.

a positive real root $0 < \lambda_r < \lambda_c$ to (3.24). As such, all asymmetric patterns of (2.21) with $N_r \geq N_\ell$ are unstable to a monotonic instability. In Figure 17(b), we show typical curves for $B(\lambda; S_\ell)$ (dashed line) and $B(\lambda; S_r)$ (solid line) for $\lambda > 0$ with $S_\ell = 3.06$ and $S_r = 6.99$. Here, $B(\lambda; S_\ell)$ crosses 0 at $\lambda_c \approx 0.65$, while $B(\lambda; S_r)$ is of constant sign. In Figure 17(c), we plot the positive real root satisfying $0 < \lambda_r < \lambda_c$ of $\mathcal{K}(\lambda)$ in the case $N_\ell = N_r = 1$. As $A|\Omega|/(4\pi(2)\sqrt{D}) \rightarrow S_{cf}^+$, the asymmetric pattern approaches a symmetric two spot pattern with $S_1 = S_2 = S_{cf}$. From the leading-order stability theory, this pattern is neutrally stable with a zero eigenvalue, consistent with Figure 17(c).

The argument above cannot, in general, be applied when $N_r < N_\ell$. Numerical solutions of $\mathcal{K}(\lambda) = 0$ in the case $N_r = 1$ and $N_\ell = 3$ (dotted branch in the right panel of Figure 5) indicate that the solution at the saddle node is neutrally stable, while the upper branch is unstable to a real positive eigenvalue. There is no positive real root of $\mathcal{K}(\lambda)$ on the lower branch, though numerical solutions of the full PDE still indicate that these solutions are monotonically unstable. This may be due to a small domain of attraction of solutions on the lower branch. A full characterization of the stability of asymmetric branches with $N_r < N_\ell$, as well as a refined stability theory for general asymmetric patterns, is beyond the scope of this paper.

3.2. Spot self-replication: A peanut-splitting instability. Next, we analyze the linear stability of a quasi-equilibrium pattern to localized radially asymmetric perturbations near each spot. Because this instability to leading order is local and does not involve coupling between spots, the same analysis applies to both symmetric and asymmetric patterns. In the j th inner region, we use the local behavior (2.17) and $\phi(\mathbf{x}_j + \varepsilon\mathbf{y}) = \Phi(\mathbf{y})$ and $\psi(\mathbf{x}_j + \varepsilon\mathbf{y}) =$

$\Psi(\mathbf{y})/D$ to write (3.2) as

$$(3.26) \quad \Delta_{\mathbf{y}}\Phi - \Phi + 2U_c V_c \Phi + V_c^2 \Psi = \lambda \Phi, \quad \Delta_{\mathbf{y}}\Psi - 2U_c V_c \Phi - V_c^2 \Psi = 0, \quad \Phi \rightarrow 0 \quad \text{as } |\mathbf{y}| \rightarrow \infty,$$

where U_c and V_c satisfy the common core problem (2.16). For (3.26), we impose the usual regularity conditions at $|\mathbf{y}| = 0$, while the far-field condition for Ψ depends on the mode of the perturbation. That is, we decompose Φ and Ψ into spherical harmonics as

$$(3.27) \quad \Phi = P_\ell^m(\cos \phi) e^{im\theta} F(\rho), \quad \Psi = P_\ell^m(\cos \phi) e^{im\theta} H(\rho),$$

where $\mathbf{y}^t = \rho(\sin \phi \cos \theta, \sin \phi \sin \theta, \cos \phi)$, with $0 < \phi < \pi$ and $0 < \theta \leq 2\pi$ being the spherical angles. In (3.27), $P_\ell^m(z)$ are the associated Legendre polynomials, ℓ is a positive integer, and $m = 0, \dots, \ell$. The $\ell = 1$ mode represents the translation mode for which $\lambda = \mathcal{O}(\varepsilon^3)$; these eigenvalues are captured in the analysis of slow spot dynamics studied in section 4. The $\ell = 0$ mode is associated with the competition instability studied in section 3. As such, we consider only the modes $\ell \geq 2$. Substituting (3.27) into (3.26), we obtain the radially symmetric eigenvalue problem

$$(3.28a) \quad \mathcal{L}_\ell F - F + 2U_c V_c \nu F + V_c^2 H = \lambda F, \quad F(0) = 0, \quad F \rightarrow 0, \quad \text{as } \rho \rightarrow \infty,$$

$$(3.28b) \quad \mathcal{L}_\ell H - 2U_c V_c F - V_c^2 H = 0, \quad H(0) = 0, \quad H \sim \frac{1}{\rho^{\ell+1}}, \quad \text{as } \rho \rightarrow \infty,$$

where we have defined the operator \mathcal{L}_ℓ by $\mathcal{L}_\ell \equiv \partial_{\rho\rho} + 2\rho^{-1}\partial_\rho - \ell(\ell+1)\rho^{-2}$. In (3.28), the boundary conditions at $\rho = 0$ are required for the regularity of $\mathcal{L}_\ell F$ and $\mathcal{L}_\ell H$ at the origin.

By solving (3.28) discretely for a range of S , we find that the eigenvalue with largest real part is real, and for each ℓ it is negative (positive) when $S < \Sigma_\ell$ ($S > \Sigma_\ell$). Here, Σ_ℓ depends on ℓ and, for the first three modes that we consider, has the ordering $\Sigma_2 < \Sigma_3 < \Sigma_4$ as shown in Figure 18. We have found that this ordering persists for the higher modes and thus see that the $\ell = 2$ mode is the dominant instability. The corresponding threshold is $\Sigma_2 \approx 20.16$. This linear instability mechanism is found numerically to trigger a nonlinear event leading to the splitting of a radially symmetric spot into two. In the analysis of localized spot patterns for the 2-D Schnakenberg model [12], this has been referred to as a ‘‘peanut-splitting instability.’’ In our 3-D case, there is a mode degeneracy in the sense that the radial modes $m = 0, 1, 2$ all lose stability simultaneously. The mode that is activated presumably depends on the initial conditions.

In terms of the original parameters of the Schnakenberg model, the splitting instability occurs when the total inhibitor feed-rate $A|\Omega|$ is sufficiently large to support more than the current number of spots, or when interaction between the spots is sufficiently weak (D is small). We remark that, in contrast to the competition mode, the peanut splitting is a local instability in that there is no leading-order coupling between the spots. That is, a particular spot will split if its strength exceeds Σ_2 , independent of the other spots. The spots of a symmetric pattern will therefore also split simultaneously if $S_c > \Sigma_2$. Together with the competition stability criterion (3.14), our leading-order asymptotic theory predicts that the symmetric quasi-equilibrium N -spot pattern is linearly stable on an $\mathcal{O}(1)$ time-scale if and

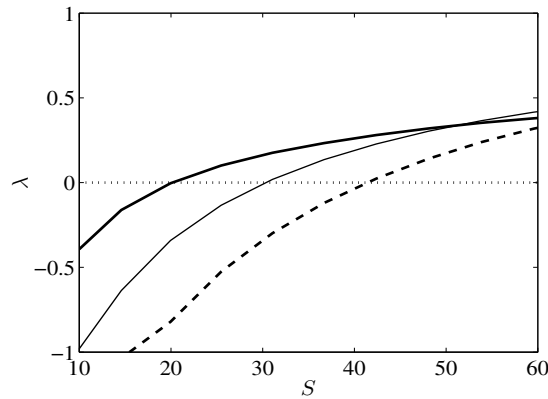


Figure 18. Plot of the eigenvalue of (3.28) with largest real part versus S for $\ell = 2$ (heavy solid line), $\ell = 3$ (light solid line), and $\ell = 4$ (heavy dashed line). As S increases, the $\ell = 2$ mode is the first to become unstable.

only if

$$(3.29) \quad S_{\text{comp}} < \frac{A|\Omega|}{4\pi N\sqrt{D}} < \Sigma_2; \quad S_{\text{comp}} \approx 4.52, \quad \Sigma_2 \approx 20.16.$$

These thresholds are equivalent to thresholds for A given in (1.3) and are in excellent agreement with numerics, as Figures 1 and 2 show.

The leading-order thresholds (1.3) provide an excellent prediction for when the splitting first starts to occur but do not predict *which spot(s)* will split. In fact, it is surprising that only one spot splits at a time. Indeed, on snapshot 7 of Figure 1 ($A = 173.248$), one can observe that at least two spots initiate the deformation (right and center spots). However, eventually only the center spot undergoes splitting. This is also very different qualitatively from both one and two dimensions. For example, in [12] the authors performed an analogous experiment in two dimensions and observed that increasing A past the threshold resulted in multiple spots splitting simultaneously. Similarly, in one dimension, multiple spots tend to replicate simultaneously [11]. A two-order expansion of S_j —see (2.35)—shows that the largest S_j corresponds to the smallest value of $(\mathcal{G}\mathbf{e})_j$. This suggests that as A is increased, the spot that self-replicates is the one with the smallest value of $(\mathcal{G}\mathbf{e})_j$. Figure 19 shows self-replication with seven spots. The value of $(\mathcal{G}\mathbf{e})_j$ is indicated for each spot in the figure. While all of these values are rather close, the self-replicating spot is indeed the one with the smallest such value (-0.27).

4. Slow spot dynamics. In this section, we analyze the slow dynamics associated with an N -spot quasi-equilibrium solution. To derive an ODE system characterizing the slow spot dynamics, we must extend the calculation in section 2 to one higher order. We will proceed by the method summarized at the end of section 2.1. In the inner region near the j th spot, we let $\mathbf{x}_j = \mathbf{x}_j(\sigma)$, where $\sigma = \varepsilon^3 t$, and expand the inner solution as

$$(4.1) \quad \mathbf{y} = \varepsilon^{-1}(\mathbf{x} - \mathbf{x}_j(\sigma)), \quad v(\mathbf{x}_j + \varepsilon\mathbf{y}) = \sqrt{D} [V_j\varepsilon(\rho) + \varepsilon^2 V_{j2}(\mathbf{y}) + \cdots], \\ u(\mathbf{x}_j + \varepsilon\mathbf{y}) = \frac{1}{\sqrt{D}} [U_j\varepsilon(\rho) + \varepsilon^2 U_{j2}(\mathbf{y}) + \cdots],$$

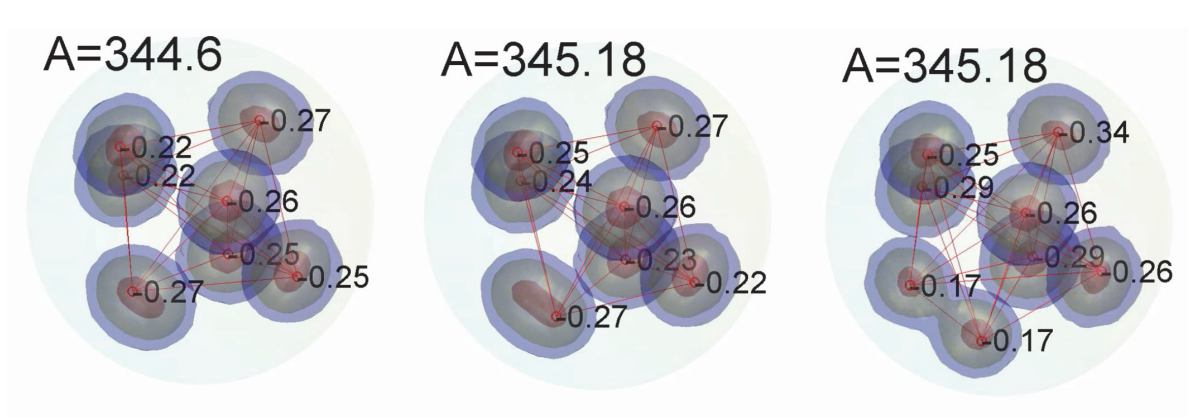


Figure 19. Numerical simulation of (1.2a) showing self-replication process of seven spots. Here $\varepsilon = 0.06$, and A is very slowly increased according to the formula $A = 200 + \varepsilon^4 t$. Snapshots show the value of A at the self-replication thresholds. Next to the spots, the value of $(\mathcal{G}\mathbf{e})_j$ is also given. Asymptotics predict that the spot with the smallest value of $(\mathcal{G}\mathbf{e})_j$ will be the one that self-replicates.

with $\rho \equiv |\mathbf{y}|$, where $U_{j\varepsilon}, V_{j\varepsilon}$ satisfy the radially symmetric core problem

$$(4.2a) \quad \Delta_\rho V_{j\varepsilon} - V_{j\varepsilon} + U_{j\varepsilon} V_{j\varepsilon}^2 = 0, \quad V'_{j\varepsilon}(0) = 0, \quad V_{j\varepsilon} \rightarrow 0, \quad \text{as } \rho \rightarrow \infty,$$

$$(4.2b) \quad \Delta_\rho U_{j\varepsilon} - U_{j\varepsilon} V_{j\varepsilon}^2 = 0, \quad U'_{j\varepsilon}(0) = 0,$$

with far-field behavior

$$(4.2c) \quad U_{j\varepsilon} \sim \mu_j - S_{j\varepsilon}/\rho + \dots, \quad \text{as } \rho \rightarrow \infty,$$

where $\mu_j \equiv \mu_0(S_{j\varepsilon})$. The corresponding outer solution (see (2.33)) is given by

$$(4.3) \quad u \sim \xi - \frac{4\pi\varepsilon}{\sqrt{D}} \sum_{i=1}^N S_{i\varepsilon} G(\mathbf{x}; \mathbf{x}_i), \quad \sum_{i=1}^N S_{i\varepsilon} = \frac{A|\Omega|}{4\pi\sqrt{D}},$$

where $S_{j\varepsilon}$, for $j = 1, \dots, N$, and ξ satisfy the nonlinear algebraic system (2.34).

We first expand u as $\mathbf{x} \rightarrow \mathbf{x}_j$, while retaining the higher-order gradient terms associated with the Green's function. Upon using (2.10b), we obtain in terms of inner variables that

$$(4.4) \quad u \sim \xi - \frac{S_{j\varepsilon}}{\sqrt{D}\rho} - \frac{4\pi\varepsilon}{\sqrt{D}} (\mathcal{G}\mathbf{S})_j - \frac{4\pi\varepsilon^2}{\sqrt{D}} \mathbf{y} \cdot \left(S_{j\varepsilon} \nabla_{\mathbf{x}} R(\mathbf{x}; \mathbf{x}_j)|_{\mathbf{x}=\mathbf{x}_j} + \sum_{\substack{i=1 \\ i \neq j}}^N S_{i\varepsilon} \nabla_{\mathbf{x}} G(\mathbf{x}; \mathbf{x}_i)|_{\mathbf{x}=\mathbf{x}_j} \right), \quad \text{as } \mathbf{x} \rightarrow \mathbf{x}_j,$$

where \mathcal{G} is the Neumann Green's matrix. The $\mathcal{O}(\varepsilon^2)$ term in (4.4) is the motivation for the form of the higher-order expansion in (4.1) and the scaling for the slow time-scale $\sigma = \varepsilon^3 t$.

Upon substituting (4.1) into (1.2) and matching the inner solution to the $\mathcal{O}(\varepsilon^2)$ term in (4.4), we obtain that $\mathbf{W}_2 = (V_{j2}, U_{j2})^T$ satisfies

$$(4.5a) \quad \mathcal{L}\mathbf{W}_2 \equiv \Delta_{\mathbf{y}} \mathbf{W}_2 + \mathcal{M}_\varepsilon \mathbf{W}_2 = - \begin{pmatrix} \mathbf{x}'_j \cdot \nabla_{\mathbf{y}} V_{j\varepsilon} \\ 0 \end{pmatrix}, \quad \mathbf{y} \in \mathbb{R}^2; \quad \mathbf{W}_2 \sim \begin{pmatrix} 0 \\ \mathbf{b}_j \cdot \mathbf{y} \end{pmatrix}, \quad \text{as } |\mathbf{y}| \rightarrow \infty.$$

Here the 2×2 matrix \mathcal{M}_ε and the vector \mathbf{b}_j are defined by (4.5b)

$$\mathcal{M}_\varepsilon \equiv \begin{pmatrix} -1 + 2U_{j\varepsilon}V_{j\varepsilon} & V_{j\varepsilon}^2 \\ -2U_{j\varepsilon}V_{j\varepsilon} & -V_{j\varepsilon}^2 \end{pmatrix}, \quad \mathbf{b}_j \equiv -4\pi S_{j\varepsilon} \nabla_{\mathbf{x}} R(\mathbf{x}; \mathbf{x}_j)|_{\mathbf{x}=\mathbf{x}_j} - 4\pi \sum_{\substack{i=1 \\ i \neq j}}^N S_{i\varepsilon} \nabla_{\mathbf{x}} G(\mathbf{x}; \mathbf{x}_i)|_{\mathbf{x}=\mathbf{x}_j}.$$

Let $\mathbf{y} = (y_1, y_2, y_3)^T$ and $\mathbf{W}_{j\varepsilon} \equiv (V_{j\varepsilon}, U_{j\varepsilon})^T$. We observe upon differentiating the core problem (4.2) with respect to i th coordinate y_i of \mathbf{y} that

$$\mathcal{L}(\partial_{y_i} \mathbf{W}_{j\varepsilon}) = 0, \quad \text{where} \quad \partial_{y_i} \mathbf{W}_{j\varepsilon} \equiv \rho^{-1} \begin{pmatrix} V_{j\varepsilon}'(\rho) \\ U_{j\varepsilon}'(\rho) \end{pmatrix} y_i, \quad \text{for } i = 1, 2, 3.$$

This shows that the dimension of the nullspace of \mathcal{L} , and consequently \mathcal{L}^* , is at least three-dimensional. We will assume that this nullspace is exactly three-dimensional, which we can verify numerically provided that $S_{j\varepsilon}$ does not coincide with the critical value $\Sigma_2 \approx 20.16$ for the peanut-splitting instability.

From a Fredholm alternative criterion, the following lemma provides a necessary condition for (4.5) to have a solution.

Lemma 4.1. *A necessary condition for (4.5) to have a solution is that $\mathbf{x}_j(\sigma)$ satisfies*

$$(4.6) \quad \mathbf{x}'_j = -\frac{3}{\kappa_1} \mathbf{b}_j, \quad \kappa_1 = \kappa_1(S_{j\varepsilon}) \equiv \int_0^\infty \rho^2 P_1(\rho) V_{j\varepsilon}'(\rho) d\rho,$$

where $P_1(\rho)$ is the first component of $\mathbf{P}(\rho) \equiv (P_1(\rho), P_2(\rho))^T$, which satisfies

$$(4.7) \quad \Delta_\rho \mathbf{P} - \frac{2}{\rho^2} \mathbf{P} + \mathcal{M}_\varepsilon^T \mathbf{P} = 0, \quad 0 < \rho < \infty; \quad \mathbf{P} \sim \begin{pmatrix} 0 \\ 1/\rho^2 \end{pmatrix}, \quad \text{as } \rho \rightarrow \infty,$$

and $\mathbf{P} = \mathcal{O}(\rho)$ as $\rho \rightarrow 0$, where $\Delta_\rho \mathbf{P} \equiv \mathbf{P}'' + 2\rho^{-1} \mathbf{P}'$.

Proof. We first seek three independent nontrivial solutions to the homogeneous adjoint problem $\mathcal{L}^* \Psi \equiv \Delta_{\mathbf{y}} \Psi + \mathcal{M}_\varepsilon^T \Psi = 0$ in the form $\Psi_i \equiv \mathbf{P}(\rho) y_i / \rho$ for $i = 1, \dots, 3$. Since

$$\Delta_{\mathbf{y}} [\mathbf{P} y_i / \rho] = \left(\Delta_\rho \mathbf{P} - \frac{2}{\rho^2} \mathbf{P} \right) \frac{y_i}{\rho},$$

we readily obtain that $\mathbf{P}(\rho)$ satisfies $\Delta_\rho \mathbf{P} - 2\rho^{-2} \mathbf{P} + \mathcal{M}_\varepsilon^T \mathbf{P} = 0$. To establish the far-field behavior of \mathbf{P} , we obtain, using (4.5b) for \mathcal{M}_ε and the fact that $V_{j0} \rightarrow 0$ exponentially as $\rho \rightarrow \infty$, that $P_2(\rho)$ satisfies $P_2'' + 2\rho^{-1} P_2' - 2\rho^{-2} P_2 \approx 0$ for $\rho \gg 1$. The decaying solution to this Euler's equation implies that $P_2 = \mathcal{O}(\rho^{-2})$ as $\rho \rightarrow \infty$, and the eigenfunction is normalized by imposing the precise behavior that $P_2 \sim 1/\rho^2$ as $\rho \rightarrow \infty$. In contrast, for $P_1(\rho)$ we obtain that $P_1'' + 2\rho^{-1} P_1' - P_1 \approx 0$ as $\rho \rightarrow \infty$, so that P_1 decays exponentially as $\rho \rightarrow \infty$. In this way, we obtain that \mathbf{P} satisfies (4.7).

Next, to derive our solvability condition we use Green's identity over a large ball of radius $|\mathbf{y}| = \rho_0 \gg 1$ to obtain that

$$(4.8) \quad \lim_{\rho_0 \rightarrow \infty} \int_{\Omega_{\rho_0}} (\Psi_i^T \mathcal{L} \mathbf{W}_2 - \mathbf{W}_2^T \mathcal{L}^* \Psi_i) d\mathbf{y} = \lim_{\rho_0 \rightarrow \infty} \int_{\partial \Omega_{\rho_0}} (\Psi_i^T \partial_\rho \mathbf{W}_2 - \mathbf{W}_2^T \partial_\rho \Psi_i) \Big|_{\rho=\rho_0} dS.$$

With $\Psi_i \equiv \mathbf{P}(\rho)y_i/\rho$, and for a fixed $i \in \{1, 2, 3\}$, we first calculate the left-hand side of this expression using (4.5a) to obtain

$$(4.9) \quad \begin{aligned} \lim_{\rho_0 \rightarrow \infty} \int_{\Omega_{\rho_0}} (\Psi_i^T \mathcal{L} \mathbf{W}_2 - \mathbf{W}_2^T \mathcal{L}^* \Psi_i) d\mathbf{y} &= - \lim_{\rho_0 \rightarrow \infty} \int_{\Omega_{\rho_0}} \frac{y_i}{\rho} P_1(\rho) (\mathbf{x}'_j \cdot \nabla_{\mathbf{y}} V_{j\varepsilon}) d\mathbf{y} \\ &= - \sum_{k=1}^3 x'_{jk} \lim_{\rho_0 \rightarrow \infty} \int_{\Omega_{\rho_0}} \frac{y_i y_k}{\rho^2} V'_{j\varepsilon}(\rho) P_1(\rho) d\mathbf{y}, \end{aligned}$$

where $\mathbf{x}'_j \equiv (x'_{j1}, x'_{j2}, x'_{j3})^T$. By using symmetry considerations, we readily establish that $\int_{\Omega_{\rho_0}} y_i y_k f(\rho) d\mathbf{y} = 0$ when $i \neq k$ and $\int_{\Omega_{\rho_0}} y_i^2 f(\rho) d\mathbf{y} = \frac{4\pi}{3} \int_0^{\rho_0} \rho^4 f(\rho) d\rho$ for any radially symmetric function $f(\rho)$. In this way, the last expression (4.9) becomes

$$(4.10) \quad \lim_{\rho_0 \rightarrow \infty} \int_{\Omega_{\rho_0}} (\Psi_i^T \mathcal{L} \mathbf{W}_2 - \mathbf{W}_2^T \mathcal{L}^* \Psi_i) d\mathbf{y} = -\frac{4\pi}{3} x'_{ji} \int_0^{\infty} \rho^2 P_1(\rho) V'_{j\varepsilon}(\rho) d\rho.$$

Next, we calculate the right-hand side of (4.8). For the first term on the right-hand side of (4.8), we use $P_2(\rho) \sim 1/\rho^2$, $U_{j1} \sim \mathbf{b}_j \cdot \mathbf{y}$, and $\partial_\rho U_{j1} \sim \mathbf{b}_j \cdot \mathbf{y}/\rho$ as $\rho \rightarrow \infty$ to estimate that

$$\lim_{\rho_0 \rightarrow \infty} \int_{\partial\Omega_{\rho_0}} \Psi_i^T \partial_\rho \mathbf{W}_2|_{\rho=\rho_0} dS = \lim_{\rho_0 \rightarrow \infty} \int_{\partial\Omega_{\rho_0}} P_2(\rho) \frac{y_i}{\rho} \partial_\rho U_{j1}|_{\rho=\rho_0} dS = \lim_{\rho_0 \rightarrow \infty} \int_{\partial\Omega_{\rho_0}} \frac{y_i}{\rho^4} (\mathbf{b}_j \cdot \mathbf{y})|_{\rho=\rho_0} dS.$$

Then, since $\int_{\partial\Omega_{\rho_0}} y_i y_k f(\rho)|_{\rho=\rho_0} dS = 0$ for $i \neq k$, and writing $dS = \rho_0^2 d\Omega_0$, where $d\Omega_0$ is the solid angle for the unit ball, we obtain that

$$(4.11) \quad \lim_{\rho_0 \rightarrow \infty} \int_{\partial\Omega_{\rho_0}} \Psi_i^T \partial_\rho \mathbf{W}_2|_{\rho=\rho_0} dS = \lim_{\rho_0 \rightarrow \infty} \int_{\partial\Omega_{\rho_0}} \frac{y_i^2}{\rho_0^2} b_{ji} d\Omega_0 = \frac{4\pi}{3} b_{ji},$$

for each $i = 1, 2, 3$. In a similar way, we can calculate the second boundary integral in (4.8) as

$$(4.12) \quad \begin{aligned} - \lim_{\rho_0 \rightarrow \infty} \int_{\partial\Omega_{\rho_0}} \mathbf{W}_2^T \partial_\rho \Psi_i|_{\rho=\rho_0} dS &= - \lim_{\rho_0 \rightarrow \infty} \int_{\partial\Omega_{\rho_0}} (\mathbf{b}_j \cdot \mathbf{y}) \partial_\rho \left[P_2(\rho) \frac{y_i}{\rho} \right] \Big|_{\rho=\rho_0} \rho_0^2 d\Omega_0 \\ &= - \lim_{\rho_0 \rightarrow \infty} \int_{\partial\Omega_{\rho_0}} (\mathbf{b}_j \cdot \mathbf{y}) \partial_\rho \left(\frac{y_i}{\rho^3} \right) \Big|_{\rho=\rho_0} \rho_0^2 d\Omega_0 \\ &= \lim_{\rho_0 \rightarrow \infty} \int_{\partial\Omega_{\rho_0}} (\mathbf{b}_j \cdot \mathbf{y}) \left(\frac{2y_i}{\rho^4} \right) \Big|_{\rho=\rho_0} \rho_0^2 d\Omega_0 \\ &= 2 \lim_{\rho_0 \rightarrow \infty} \int_{\partial\Omega_{\rho_0}} b_{ji} \frac{y_i^2}{\rho_0^2} \Big|_{\rho=\rho_0} d\Omega_0 = \frac{8\pi}{3} b_{ji}. \end{aligned}$$

By adding (4.11) and (4.12), we obtain that the right-hand side of (4.8) is $4\pi b_{ji}$. Finally, by equating this expression with that given in (4.10) for the left-hand side of (4.8), we obtain that $x'_{ji} = -3b_{ji}/\kappa_1$, where κ_1 is defined in (4.6). In vector form, with $i = 1, 2, 3$, we obtain (4.6). ■

By combining (4.6) with our expression for \mathbf{b}_j in (4.5b), we obtain an ODE–DAE system for the slow spot dynamics given by

$$(4.13) \quad \frac{d\mathbf{x}_j}{dt} = \frac{12\pi\varepsilon^3}{\kappa_1} \left(S_{j\varepsilon} \nabla_{\mathbf{x}} R(\mathbf{x}; \mathbf{x}_j)|_{\mathbf{x}=\mathbf{x}_j} + \sum_{\substack{i=1 \\ i \neq j}}^N S_{i\varepsilon} \nabla_{\mathbf{x}} G(\mathbf{x}; \mathbf{x}_i)|_{\mathbf{x}=\mathbf{x}_j} \right), \quad j = 1, \dots, N,$$

where $\kappa_1 = \kappa_1(S_{j\varepsilon})$ and $S_{1\varepsilon}, \dots, S_{N\varepsilon}$ are determined from the nonlinear algebraic system (2.34), which for $\varepsilon \ll 1$ depends weakly on the spot locations $\mathbf{x}_1, \dots, \mathbf{x}_N$. This ODE–DAE system is valid when the N -spot quasi-equilibrium pattern is linearly stable to either competition or peanut-splitting instabilities, as was discussed in section 3. Our numerical computations of κ_1 shown in Figure 20(a) reveal that $\kappa_1 < 0$ for $0 < S_j < \Sigma_2 \approx 20.16$.

Numerical realizations of the ODE–DAE system (4.13) and (2.34) are readily possible when Ω is the unit ball. In this special case, the Neumann Green’s function and its regular part were given explicitly in (2.11). Since $G(\mathbf{x}; \boldsymbol{\xi}) = G(\boldsymbol{\xi}; \mathbf{x})$, we can write (2.11) as

$$(4.14) \quad G(\mathbf{x}; \boldsymbol{\xi}) = \frac{1}{4\pi} \left(\frac{1}{|\mathbf{x} - \boldsymbol{\xi}|} + \frac{1}{|\boldsymbol{\xi}|} \frac{1}{|\mathbf{x} - \boldsymbol{\xi}'|} \right) - \frac{1}{4\pi} \log(\mathcal{T}) + \frac{1}{8\pi} |\mathbf{x}|^2 + h(\boldsymbol{\xi}), \quad \mathcal{T} \equiv (\boldsymbol{\xi}' - \mathbf{x}) \cdot \frac{\boldsymbol{\xi}}{|\boldsymbol{\xi}|} + |\boldsymbol{\xi}' - \mathbf{x}|,$$

for some $h(\boldsymbol{\xi})$, where $\boldsymbol{\xi}' \equiv \boldsymbol{\xi}/|\boldsymbol{\xi}|^2$. A simple calculation of the gradient, which is needed in (4.13), yields

$$(4.15a) \quad \nabla_{\mathbf{x}} G(\mathbf{x}; \boldsymbol{\xi}) = -\frac{1}{4\pi} \left(\frac{\mathbf{x} - \boldsymbol{\xi}}{|\mathbf{x} - \boldsymbol{\xi}|^3} + \frac{1}{|\boldsymbol{\xi}|} \frac{\mathbf{x} - \boldsymbol{\xi}'}{|\mathbf{x} - \boldsymbol{\xi}'|^3} \right) + \frac{1}{4\pi\mathcal{T}} \left(\frac{\boldsymbol{\xi}}{|\boldsymbol{\xi}|} + \frac{\boldsymbol{\xi}' - \mathbf{x}}{|\mathbf{x} - \boldsymbol{\xi}'|} \right) + \frac{\mathbf{x}}{4\pi},$$

$$(4.15b) \quad \nabla_{\mathbf{x}} R(\mathbf{x}; \boldsymbol{\xi}) = -\frac{1}{4\pi} \frac{1}{|\boldsymbol{\xi}|} \frac{\mathbf{x} - \boldsymbol{\xi}'}{|\mathbf{x} - \boldsymbol{\xi}'|^3} + \frac{1}{4\pi\mathcal{T}} \left(\frac{\boldsymbol{\xi}}{|\boldsymbol{\xi}|} + \frac{\boldsymbol{\xi}' - \mathbf{x}}{|\mathbf{x} - \boldsymbol{\xi}'|} \right) + \frac{\mathbf{x}}{4\pi}.$$

For a particular parameter set, as described in the caption of Figure 20(b), we compare results from (4.13) for a two spot evolution in the ball with corresponding full numerical results computed from the PDE (1.2) using FlexPDE6 [6]. In our example, the two spots are initially taken to be in an antipodal configuration so that $\mathbf{e} = (1, 1)^T$ is an eigenvector of the Green’s matrix \mathcal{G} . As a result, from (2.36) we have $S_{1\varepsilon} = S_{2\varepsilon} \equiv S_c = A/(6\sqrt{D})$. The results shown in Figure 20(b) show that the asymptotic result (4.13) is highly accurate in predicting the full dynamics. For this special configuration, we obtain from (4.13) and (4.15) that $\mathbf{x}_1 = (0, 0, z_0)$ and $\mathbf{x}_2 = -\mathbf{x}_1$, where z_0 satisfies the explicit ODE

$$(4.16) \quad \frac{dz_0}{dt} = -\frac{3S_c\varepsilon^3}{|\kappa_1|} \mathcal{F}_2(z_0), \quad \mathcal{F}_2(z_0) \equiv \frac{2z_0^3(3 - z_0^4)}{(z_0^4 - 1)^2} + 2z_0 - \frac{1}{4z_0^2}.$$

It is readily verified that there is a unique root z_{0e} to $\mathcal{F}_2(z_0) = 0$ on $0 < z_0 < 1$, and using a root finder we get $z_{0e} \approx 0.42885$, which confirms the result shown in Figure 20.

For an arbitrary initial configuration of spots, we recall from (2.35) that to leading order in ε we have $S_j = S_c + \mathcal{O}(\varepsilon)$, where S_c is given in (2.14). Then, upon introducing the discrete energy $\mathcal{H}(\mathbf{x}_1, \dots, \mathbf{x}_N)$ defined by

$$(4.17) \quad \mathcal{H}(\mathbf{x}_1, \dots, \mathbf{x}_N) \equiv \sum_{i=1}^N R(\mathbf{x}_i; \mathbf{x}_i) + 2 \sum_{i=1}^N \sum_{j>i}^N G(\mathbf{x}_i; \mathbf{x}_j),$$

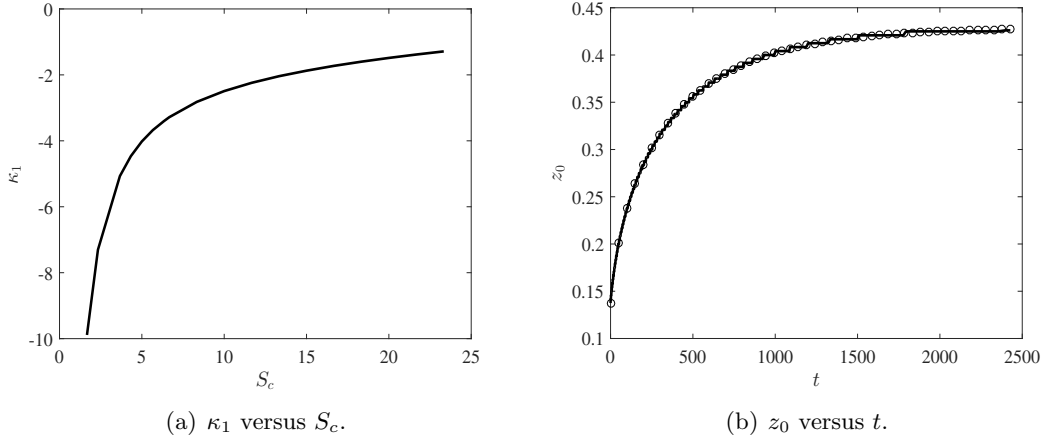


Figure 20. (a) κ_1 versus S_c computed numerically from (4.6), which shows that $\kappa_1 < 0$ for $0 < S_c < \Sigma_2 \approx 20.16$. (b) Plot of the z -coordinate $z_0(t) > 0$ of two antipodal spots initially located at $(0, 0, \pm 0.1375)$. The other spot evolves as $-z_0(t)$. The solid curve is obtained from numerically solving the full Schnakenberg model (1.2) in the unit ball, while the circles are obtained from numerically solving the ODE (4.16), as derived from (4.13), with $S_{1\varepsilon} = S_{2\varepsilon} = A/(6\sqrt{D})$. The parameters are $D = 1$, $A = 80$, and $\varepsilon = 0.02$. For this parameter set, where $S_{1\varepsilon} \approx 13.33$, we get $\kappa_1 = -2.0395$.

we can write (4.13) in the form of a gradient flow. The result is summarized as follows.

Main Result 4.2. *Let $\varepsilon \rightarrow 0$, and suppose that the N -spot quasi-equilibrium solution of (1.2) is linearly stable on an $\mathcal{O}(1)$ time-scale to either competition or peanut-splitting instabilities. Then to leading order in ε , the collection of spots evolves by the gradient flow*

$$(4.18) \quad \frac{d\mathbf{x}_j}{dt} = -\frac{6\pi\varepsilon^3 S_c}{|\kappa_1|} \nabla_{\mathbf{x}_j} \mathcal{H}(\mathbf{x}_1, \dots, \mathbf{x}_N), \quad j = 1, \dots, N; \quad S_c = \frac{A|\Omega|}{4\pi N\sqrt{D}},$$

where the discrete energy \mathcal{H} is defined in (4.17). Here $\kappa_1 = \kappa_1(S_c)$ is defined in (4.6). In terms of the spatial configuration $\{\mathbf{x}_1, \dots, \mathbf{x}_N\}$ of spots, a two-term expansion for the spot strengths when $\mu'_0(S_c) \neq 0$ is

$$(4.19) \quad S_{j\varepsilon} \sim S_c + \frac{4\pi\varepsilon S_c}{\mu'_0(S_c)} \left(\frac{\mathbf{e}^T \mathcal{G} \mathbf{e}}{N} - (\mathcal{G} \mathbf{e})_j \right) + \dots, \quad j = 1, \dots, N,$$

where $\mathbf{e} = (1, \dots, 1)^T$ and \mathcal{G} is the Neumann Green's matrix.

We now use (4.18) to discuss possible steady-state spot configurations. It follows from (4.18) that spatial configurations of steady-state spots are critical points of the discrete energy \mathcal{H} , and that patterns that are linearly stable with respect to the ODE dynamics (4.18) are minima of \mathcal{H} . The discrete energy \mathcal{H} also arises in the analysis of the MFPT for a Brownian walk in a 3-D domain with small localized spherical traps (cf. [3]). Following the decomposition in [3], we define \mathcal{H}_0 by

$$(4.20) \quad \mathcal{H}(\mathbf{x}_1, \dots, \mathbf{x}_N) = \frac{\mathcal{H}_0}{4\pi} - \frac{7N^2}{10\pi}, \quad \mathcal{H}_0 \equiv 4\pi \left[\sum_{i=1}^N \left(R(\mathbf{x}_i; \mathbf{x}_i) + \frac{7}{10\pi} \right) + 2 \sum_{i=1}^N \sum_{j>i}^N \left(G(\mathbf{x}_i; \mathbf{x}_j) + \frac{7}{10\pi} \right) \right].$$

Table 1

Numerically computed minimal values of the discrete energy function \mathcal{H}_0 for the optimal arrangement of N -traps within a unit ball where the optimization is restricted to a one-ring configuration $\mathcal{H}_0^{(a)}$, or to a one-ring configuration with a center spot $\mathcal{H}_0^{(b)}$ (see [3]). The minimum of these two values is shown in boldface. The unrestricted optimization of \mathcal{H}_0 gives results extremely close to the restricted minimum energies in this table, but that not all spots lie exactly on a ring of a common radius.

N	$\mathcal{H}_0^{(a)}$	Spherical radii $r_j = r_c$ for all j	$\mathcal{H}_0^{(b)}$	Spherical radii $r_j = r_c$ for all j , ($r_1 = 0$)
2	7.2763	0.429	9.0316	0.563
3	18.5047	0.516	20.3664	0.601
4	34.5635	0.564	36.8817	0.626
5	56.2187	0.595	58.1823	0.645
6	82.6490	0.618	85.0825	0.659
7	115.016	0.639	116.718	0.671
8	152.349	0.648	154.311	0.680
9	195.131	0.659	196.843	0.688
10	243.373	0.668	244.824	0.694
11	297.282	0.676	297.283	0.700
12	355.920	0.683	357.371	0.705
13	420.950	0.689	421.186	0.710
14	491.011	0.694	491.415	0.713
15	566.649	0.698	566.664	0.717
16	647.738	0.702	647.489	0.720
17	734.344	0.706	733.765	0.722
18	826.459	0.709	825.556	0.725
19	924.360	0.712	922.855	0.727
20	1027.379	0.715	1025.94	0.729

For the unit ball, in Table 1 we give some results for $N = 2, \dots, 20$ computed in [3] using numerical optimization software for a restricted optimization problem, whereby \mathcal{H}_0 is minimized subject to the condition that either all N spots must be on a single ring (second and third columns) or all $N - 1$ points are on a single ring while the remaining spot is at the origin (fourth and fifth columns). From this table we observe for $N \geq 16$ that the second class of patterns gives a smaller \mathcal{H}_0 . It was found in [3] that, for $N = 2, \dots, 20$, an unrestricted optimization of \mathcal{H}_0 gives results that coincide to the number of digits shown with the restricted minimum energies in Table 1, with all spots being very close to, but not exactly on, a common ring of radius r_c . As a result, for $N = 2, \dots, 20$, the global minimum of \mathcal{H}_0 can be predicted rather accurately from the restricted optimization results in Table 1.

Point configurations corresponding to such global minima of \mathcal{H}_0 are linearly stable equilibria of the ODE dynamics (4.18). We then perform numerical simulations of (4.18) with randomly generated initial conditions in an attempt to classify steady-states of (4.18) with large basins of attraction of initial conditions. We find for $N = 2, 3, 4, 6, 8$ that the computed steady-state solutions agree precisely with those for the one-ring patterns shown in the second and third columns in Table 1 and that, for these values of N , $\mathbf{e} = (1, \dots, 1)^T$ is an eigenvector

of the Green's matrix \mathcal{G} at the steady-state. In particular, for $N = 2$, the first row of Table 1 predicts that a two spot steady-state of (4.18) will correspond to antipodal spots on an interior ball of radius $r_c \approx 0.429$, which is precisely what was observed in the results shown in Figure 20(b). In addition, for $N = 4$ we observe from Table 1 that the bifurcation diagram shown in Figure 7(a) corresponds to true steady-state solutions. Moreover, our numerical results show for $N = 12$ that some initial conditions for (4.18) lead to a steady-state where the spots are centered at the vertices of an icosahedron with discrete energy and radius given in Table 1, for which \mathbf{e} is an eigenvector of \mathcal{G} , while other initial conditions lead to a pattern with 11 spots nearly on a common ring with a spot at the center. For $N = 13, 14, 15$, initial conditions lead either to spots nearly on a common ring or to the near-ring and center-hole pattern. For $N = 16, \dots, 20$ our computations of (4.18) lead typically to the near-ring and center-hole pattern. For $N = 12, \dots, 20$, we find that the discrete energies at the steady-state coincide very closely with the restricted optimization results in Table 1. For $N = 5$, our simulations of (4.18) with random initial conditions show that (4.18) converges to a steady-state with two antipodal spots at a distance of 0.59279 from the origin, and with three spots equally spaced on a midplane with spots being at a distance of 0.59605 from the origin.

4.1. Spot dynamics with a spatially varying feed-rate. In this subsection we extend our previous analysis of (1.2) to the case where the feed-rate A depends on \mathbf{x} , with $A(\mathbf{x}) > 0$ in Ω . We only briefly highlight the new features of the analysis needed when $A = A(\mathbf{x})$.

We proceed by the method discussed at the end of section 2.1. Since the inner solution near each spot does not depend on A , we can proceed as in section 2.1 to allow the source strength S_j in (2.2) to depend weakly on ε , and so we write $U_{j\varepsilon}, V_{j\varepsilon}$ to be the solution to (2.2) for which $U_{j\varepsilon} \sim \mu_j - S_{j\varepsilon}/\rho$ as $\rho \rightarrow \infty$, where $\mu_j \equiv \mu_0(S_{j\varepsilon})$. In place of (2.32), the outer solution now satisfies

$$(4.21) \quad \Delta u \sim -\frac{\varepsilon A(\mathbf{x})}{D} + \frac{4\pi\varepsilon}{\sqrt{D}} \sum_{j=1}^N S_{j\varepsilon} \delta(\mathbf{x} - \mathbf{x}_j), \quad \mathbf{x} \in \Omega; \quad \partial_n u = 0, \quad \mathbf{x} \in \partial\Omega.$$

By the divergence theorem, we obtain that

$$(4.22) \quad \sum_{i=1}^N S_{i\varepsilon} = \frac{\bar{A}|\Omega|}{4\pi\sqrt{D}}, \quad \bar{A} \equiv \frac{1}{|\Omega|} \int_{\Omega} A(\mathbf{x}) d\mathbf{x}.$$

The exact solution to (4.21) is simply

$$(4.23) \quad u = \xi + \frac{\varepsilon}{D} u_{1p}(\mathbf{x}) - \frac{4\pi\varepsilon}{\sqrt{D}} \sum_{i=1}^N S_{i\varepsilon} G(\mathbf{x}; \mathbf{x}_i),$$

where ξ is a constant, G is the Neumann Green's function of (2.10), and $u_{1p}(\mathbf{x})$ is the unique solution to

$$(4.24) \quad \Delta u_{1p} = -A(\mathbf{x}) + \bar{A}, \quad \mathbf{x} \in \Omega; \quad \partial_n u_{1p} = 0, \quad \mathbf{x} \in \partial\Omega; \quad \int_{\Omega} u_{1p} d\mathbf{x} = 0,$$

which is given explicitly by

$$(4.25) \quad u_{1p}(\mathbf{x}) = \int_{\Omega} G(\boldsymbol{\xi}; \mathbf{x}) A(\boldsymbol{\xi}) d\boldsymbol{\xi}.$$

By expanding (4.23) as $\mathbf{x} \rightarrow \mathbf{x}_j$ we obtain in terms of inner variables that

$$(4.26) \quad u \sim \xi - \frac{S_{j\varepsilon}}{\sqrt{D}\rho} + \frac{\varepsilon}{D} u_{1p}(\mathbf{x}_j) - \frac{4\pi\varepsilon}{\sqrt{D}} (\mathcal{G}\mathbf{S})_j + \frac{\varepsilon^2}{\sqrt{D}} \mathbf{y} \cdot \tilde{\mathbf{b}}_j + \dots, \quad \text{as } \mathbf{x} \rightarrow \mathbf{x}_j,$$

where \mathcal{G} is the Neumann Green's matrix, $\mathbf{S} \equiv (S_{1\varepsilon}, \dots, S_{N\varepsilon})^T$, and where we have defined $\tilde{\mathbf{b}}_j$ by

$$(4.27) \quad \tilde{\mathbf{b}}_j \equiv \frac{1}{\sqrt{D}} \nabla_{\mathbf{x}} u_{1p}|_{\mathbf{x}=\mathbf{x}_j} - 4\pi \left(S_{j\varepsilon} \nabla_{\mathbf{x}} R(\mathbf{x}; \mathbf{x}_j)|_{\mathbf{x}=\mathbf{x}_j} + \sum_{\substack{i=1 \\ i \neq j}}^N S_{i\varepsilon} \nabla_{\mathbf{x}} G(\mathbf{x}; \mathbf{x}_i)|_{\mathbf{x}=\mathbf{x}_j} \right).$$

Upon matching (4.26) to the far-field behavior of the j th inner solution defined in (4.1) we obtain, in place of (2.34), that $S_{j\varepsilon}$, for $j = 1, \dots, N$, and ξ now satisfy

$$(4.28) \quad \xi - \frac{4\pi\varepsilon}{\sqrt{D}} (\mathcal{G}\mathbf{S})_j + \frac{\varepsilon}{D} u_{1p}(\mathbf{x}_j) = \frac{\mu_0(S_{j\varepsilon})}{\sqrt{D}}, \quad j = 1, \dots, N; \quad \sum_{j=1}^N S_{j\varepsilon} = \frac{\bar{A}|\Omega|}{4\pi\sqrt{D}},$$

where the graph of $\mu_0(S_{j\varepsilon})$ versus $S_{j\varepsilon}$ was shown in Figure 3(a). In addition, we obtain that $\mathbf{W}_2 = (V_{j2}, U_{j2})^T$ now satisfies (4.5) with \mathbf{b}_j replaced by $\tilde{\mathbf{b}}_j$. Therefore, by using Lemma 4.1 we can determine the slow spot dynamics in terms of $\tilde{\mathbf{b}}_j$. This yields, in place of (4.13), that the ODE–DAE system for the slow spot dynamics when $A = A(\mathbf{x})$ is, for each $j = 1, \dots, N$,

$$(4.29) \quad \frac{d\mathbf{x}_j}{dt} = -\frac{\varepsilon^3}{\kappa_1} \left[\frac{3}{\sqrt{D}} \nabla_{\mathbf{x}} u_{1p}|_{\mathbf{x}=\mathbf{x}_j} - 12\pi \left(S_{j\varepsilon} \nabla_{\mathbf{x}} R(\mathbf{x}; \mathbf{x}_j)|_{\mathbf{x}=\mathbf{x}_j} + \sum_{\substack{i=1 \\ i \neq j}}^N S_{i\varepsilon} \nabla_{\mathbf{x}} G(\mathbf{x}; \mathbf{x}_i)|_{\mathbf{x}=\mathbf{x}_j} \right) \right],$$

where $S_{1\varepsilon}, \dots, S_{N\varepsilon}$ are now determined from the nonlinear algebraic system (4.28), and $\kappa_1 = \kappa_1(S_{j\varepsilon}) < 0$ from Figure 20(a). Finally, upon making the leading-order approximation $S_j = S_c + \mathcal{O}(\varepsilon)$, for $j = 1, \dots, N$, where

$$(4.30) \quad S_c = \frac{\bar{A}|\Omega|}{4\pi N\sqrt{D}},$$

we can readily reduce (4.29) to the following simple result.

Main Result 4.3. *Let $\varepsilon \rightarrow 0$, and suppose that the N -spot quasi-equilibrium solution of (1.2) with $A = A(\mathbf{x}) > 0$ is linearly stable on an $\mathcal{O}(1)$ time-scale to either competition or peanut-splitting instabilities. Then, to leading order in ε , the slow time evolution of the collection of spots satisfies, for each $j = 1, \dots, N$,*

$$(4.31) \quad \frac{d\mathbf{x}_j}{dt} = -\frac{12\pi S_c \varepsilon^3}{|\kappa_1|} \left(\nabla_{\mathbf{x}} R(\mathbf{x}; \mathbf{x}_j)|_{\mathbf{x}=\mathbf{x}_j} + \sum_{\substack{i=1 \\ i \neq j}}^N \nabla_{\mathbf{x}} G(\mathbf{x}; \mathbf{x}_i)|_{\mathbf{x}=\mathbf{x}_j} - \frac{N}{\bar{A}|\Omega|} \nabla_{\mathbf{x}} u_{1p}|_{\mathbf{x}=\mathbf{x}_j} \right),$$

where S_c is given in (4.30). In terms of the discrete energy \mathcal{H} of (4.17), we have equivalently that

$$(4.32) \quad \frac{d\mathbf{x}_j}{dt} = -\frac{6\pi S_c \varepsilon^3}{|\kappa_1|} \left(\nabla_{\mathbf{x}_j} \mathcal{H}(\mathbf{x}_1, \dots, \mathbf{x}_N) - \frac{2N}{\bar{A}|\Omega|} \nabla_{\mathbf{x}} u_{1p}|_{\mathbf{x}=\mathbf{x}_j} \right), \quad j = 1, \dots, N,$$

where u_{1p} , which satisfies (4.24), is given explicitly in (4.25). Here $\kappa_1 = \kappa_1(S_c) < 0$ is defined in (4.6) (see Figure 20(a)). In terms of the spatial configuration $\{\mathbf{x}_1, \dots, \mathbf{x}_N\}$ of spots, a two-term expansion for the source strengths when $\mu'_0(S_c) \neq 0$, as obtained from (4.28), is

$$(4.33) \quad S_{j\varepsilon} \sim S_c + \frac{4\pi\varepsilon S_c}{\mu'_0(S_c)} \left(\frac{\mathbf{e}^T \mathcal{G} \mathbf{e}}{N} - (\mathcal{G} \mathbf{e})_j \right) + \frac{\varepsilon}{\sqrt{D} \mu'_0(S_c)} \left(u_{1p}(\mathbf{x}_j) - \frac{1}{N} \sum_{i=1}^N u_{1p}(\mathbf{x}_i) \right), \quad j = 1, \dots, N,$$

where $\mathbf{e} = (1, \dots, 1)^T$ and \mathcal{G} is the Neumann Green's matrix.

We now illustrate Main Result 4.3 for a few choices of the variable feed A in the unit ball.

Example 1 (radially symmetric feed-rate: $A = A(r)$). We first use (4.31) to derive an ODE for a one spot solution centered at $\mathbf{x}_1 = (r, 0, 0)$ along the positive x axis inside a unit ball when the feed-rate A is purely radial, i.e., $A = A(r)$. We use $S_c = \bar{A}/(3\sqrt{D})$ from (4.30), together with (4.15) and the solution u_{1p} to (4.24), to readily obtain that (4.31) reduces to

$$(4.34) \quad \frac{dr}{dt} = -\frac{\bar{A}\varepsilon^3}{\sqrt{D}|\kappa_1|} \mathcal{F}_{1a}(r), \quad \text{where} \quad \mathcal{F}_{1a}(r) \equiv \frac{r(2-r^2)}{(1-r^2)^2} + \frac{3}{\bar{A}r^2} \int_0^r A(\rho) \rho^2 d\rho,$$

and $\bar{A} = 3 \int_0^1 \rho^2 A(\rho) d\rho$. Since $\mathcal{F}_{1a}(0) = 0$, $r = 0$ is always an equilibrium point. Moreover, since $\mathcal{F}_{1a}(r) \sim r [2 + A(0)/\bar{A}] > 0$ as $r \rightarrow 0$, it follows that $r = 0$ is a stable equilibrium point of the ODE (4.34) for any $A(r) > 0$. Finally, since $\mathcal{F}_{1a}(r) > 0$ on $0 < r < 1$, we conclude that there is no radially symmetric feed-rate that can lead to the pinning of a spot at some distance r_e , with $0 < r_e < 1$, from the origin.

Next, we consider a two spot pattern in a spherical domain where the spots are symmetrically placed at $\mathbf{x}_1 = (r, 0, 0)$ and $\mathbf{x}_2 = -\mathbf{x}_1$ with $0 < r < 1$. Assume that $A = A(r) > 0$. We use $S_c = \bar{A}/(6\sqrt{D})$ from (4.30), together with (4.15) and the solution u_{1p} to (4.24), to readily obtain that (4.31) reduces to

$$(4.35) \quad \frac{dr}{dt} = -\frac{3S_c \varepsilon^3}{|\kappa_1|} \mathcal{F}_{2a}(r), \quad \mathcal{F}_{2a}(r) \equiv \frac{2r^3(3-r^4)}{(r^4-1)^2} + r - \frac{1}{4r^2} + \frac{3}{r^2 \bar{A}} \int_0^r A \rho^2 d\rho,$$

where $\bar{A} = 3 \int_0^1 \rho^2 A(\rho) d\rho$. Any steady-state r_{0e} of (4.35) must satisfy

$$(4.36) \quad \frac{2r^5(3-r^4)}{(r^4-1)^2} + \frac{\int_0^r \rho^2 A(\rho) d\rho}{\int_0^1 \rho^2 A(\rho) d\rho} = \frac{1}{4} - r^3.$$

The left-hand side of (4.36) is monotone increasing, is zero at $r = 0$, and is unbounded as $r \rightarrow 1^-$. Since the right-hand side is monotone decreasing on $0 < r < 1$ and has a unique sign change at $r = 4^{-1/3}$, it follows that there is a unique steady-state solution r_{0e} to (4.35) on $0 < r_{0e} < 4^{-1/3}$ for any $A(\rho) > 0$. Therefore, the effect of the radially symmetric feed-rate is simply to modify the location of the steady-state observed in Figure 20 for the case where A was constant.

Example 2 (pinning of a spot). We consider a one spot solution and take $A(\mathbf{x}) = A_0 + Bz$ with $0 < B < A_0$, where $\mathbf{x} = (x, y, z)^T$. For this case, $\bar{A} = A_0$, and we calculate from (4.24) that

$$(4.37) \quad u_{1p}(\mathbf{x}) = \frac{Bz}{10} (3 - |\mathbf{x}|^2), \quad \nabla_{\mathbf{x}} u_{1p}(\mathbf{x}) = \frac{B}{10} (-2xz, -2yz, 3 - |\mathbf{x}|^2 - 2z^2)^T.$$

We obtain from (4.15b) that

$$(4.38) \quad \nabla_{\mathbf{x}} R(\mathbf{x}; \mathbf{x}_1)|_{\mathbf{x}=\mathbf{x}_1} = \frac{\mathbf{x}_1}{4\pi} \left[\frac{2 - r^2}{(1 - r^2)^2} + 1 \right],$$

so that (4.31) with $N = 1$ and u_{1p} as in (4.37) yields that

$$(4.39) \quad \frac{d\mathbf{x}_1}{dt} = -\frac{3\varepsilon^3 S_1}{|\kappa_1|} \left[\mathbf{x}_1 \left(\frac{(2 - r^2)}{(1 - r^2)^2} + 1 \right) + \frac{3B}{10A_0} (2x_1 z_1, 2y_1 z_1, -3 + r^2 + 2z_1^2)^T \right],$$

where $r = |\mathbf{x}_1|$ and $S_1 = A_0/(3\sqrt{D})$. The steady-state for (4.39) is $x_{1e} = y_{1e} = 0$, while $z_{1e} = r_e$ is the unique root on $0 < r_e < 1$ of

$$(4.40) \quad r \left(\frac{(2 - r^2)}{(1 - r^2)^2} + 1 \right) = \frac{9B}{10A_0} (1 - r^2),$$

which can be found numerically. In particular, if $A_0 = 40$ and $B = 20$ so that $A(\mathbf{x}) = 40(1 + z/2)$, the unique equilibrium point is $(x_{1e}, y_{1e}, z_{1e})^T = (0, 0, 0.14387)^T$. Therefore, in this case we predict that the variable feed-rate leads to an equilibrium spot solution on the positive z axis in the direction where the feed is largest. For $\varepsilon = 0.03$ and the initial location $\mathbf{x}_1(0) = (0.4, 0.5, 0.3)^T$, this is confirmed in Figure 21(a) from a FlexPDE6 [6] full numerical computation of (1.2). We remark that the full numerical results in Figure 21(a) compare very favorably with results from the ODE (4.39).

Example 3 (pinning of a spot by a localized source of feed). Finally, we consider one spot dynamics for the case where the variable feed-rate has a background state that is augmented by a localized source where the feed is large. As a model for this situation we take

$$(4.41) \quad A(\mathbf{x}) = A_0 + B\delta(\mathbf{x} - \boldsymbol{\xi}),$$

where $A_0 > 0$, $B > 0$, and $\boldsymbol{\xi} \in \Omega$. We calculate $\bar{A} = A_0 + B/|\Omega|$, and the solution to (4.24) is $u_{1p}(\mathbf{x}) = BG(\mathbf{x}; \boldsymbol{\xi})$. From (4.31) and (4.15), we obtain that the one spot dynamics is

$$(4.42) \quad \frac{d\mathbf{x}_1}{dt} = -\frac{3\varepsilon^3 S_1}{|\kappa_1|} \left[\mathbf{x}_1 \left(\frac{(2 - r^2)}{(1 - r^2)^2} + 1 \right) - \frac{3B}{A_0 + B/|\Omega|} \nabla_{\mathbf{x}} G(\mathbf{x}; \boldsymbol{\xi})|_{\mathbf{x}=\mathbf{x}_1} \right],$$

with $S_1 = (A_0 + B/|\Omega|)/(3\sqrt{D})$, and where $\nabla_{\mathbf{x}} G(\mathbf{x}; \boldsymbol{\xi})|_{\mathbf{x}=\mathbf{x}_1}$ can be calculated from (4.15a). Due to the $1/r$ singularity in G , it follows from (4.42) that if the initial point $\mathbf{x}_1(0)$ is sufficiently close to the source $\boldsymbol{\xi}$ of the feed, then we claim that $\mathbf{x}_1(T) = \boldsymbol{\xi}$ at some $t = T < \infty$. To see this, we observe from (4.42) and (4.15a) that for \mathbf{x}_1 near $\boldsymbol{\xi}$, we have $d\mathbf{x}_1/dt \sim -c(\mathbf{x}_1 - \boldsymbol{\xi})/|\mathbf{x}_1 - \boldsymbol{\xi}|^3$ for some $c > 0$, which implies that $|\mathbf{x}_1 - \boldsymbol{\xi}| \sim (3c)^{1/3}(T - t)^{1/3}$ for t near T .

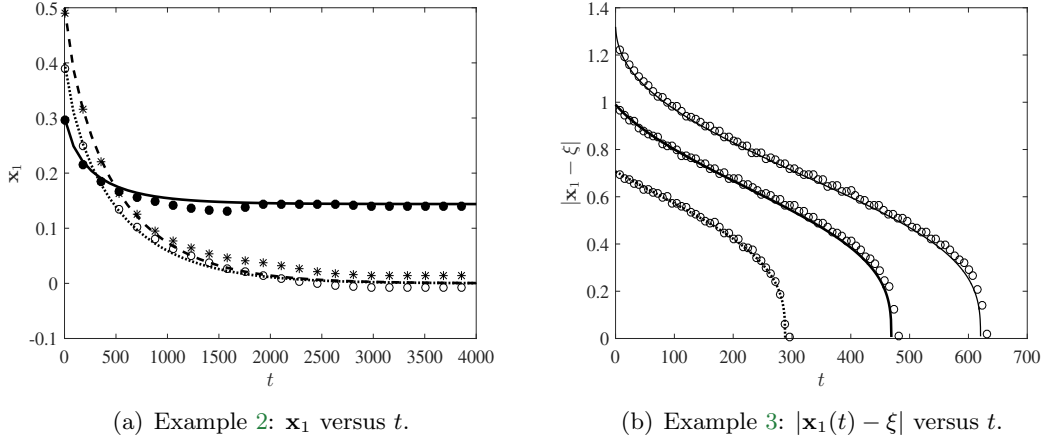


Figure 21. (a) Plot of the full numerical results (discrete points) computed from (1.2) using FlexPDE6 [6] for the three components of the spot trajectory \mathbf{x}_1 versus t for Example 2 where $A(\mathbf{x}) = 40 + 20z$, $D = 1$, $\varepsilon = 0.03$, and with initial condition $\mathbf{x}_1(0) = (0.4, 0.5, 0.3)^T$. The three curves are the asymptotic result (4.39) with the labels x (dotted line), y (dashed line), and z (solid line), where $\mathbf{x}_1 = (x, y, z)^T$. The results confirm that $\mathbf{x}_1 \rightarrow (0, 0, 0.14387)^T$ as $t \rightarrow \infty$. (b) Numerical solutions of the ODE (4.42) (continuous curves) for Example 3 where $A(\mathbf{x})$ is given in (4.41) with $D = 1$ and $\varepsilon = 0.03$. The discrete points are full numerical results computed from (1.2) using FlexPDE6 [6]. The parameters are $A_0 = 20$ and $B = 20|\Omega|$, with $|\Omega| = 4\pi/3$. The localized feed is at $\boldsymbol{\xi} = (0, 0, 0.5)$, and we plot the distance $|\mathbf{x}_1(t) - \boldsymbol{\xi}|$ versus t for three initial conditions: $\mathbf{x}_1(0) = (0, 0.7, -0.2)^T$ (heavy solid curve), $\mathbf{x}_1(0) = (-0.7, -0.2, -0.6)^T$ (solid curve), and $\mathbf{x}_1(0) = (-0.5, 0.0, 0.0)^T$ (dotted curve).

This finite-time pinning phenomenon is shown in Figure 21(b) where we plot the distance $|\mathbf{x}_1(t) - \boldsymbol{\xi}|$ versus t for a one spot solution in the unit ball for the parameter set $A_0 = 20$, $B = 20|\Omega|$, $D = 1$, and $\varepsilon = 0.03$. In this figure we show a very favorable comparison between results computed from the asymptotic ODE (4.42) and the full numerical solution to (1.2) using FlexPDE6 [6] for three different initial conditions $\mathbf{x}_1(0)$. When using FlexPDE6 on (1.2) for $A(\mathbf{x})$ given in (4.41), we mollified the delta singularity by using the following 3-D Gaussian approximation with $\sigma = 0.005$:

$$A(\mathbf{x}) = A_0 + BF(|\mathbf{x} - \boldsymbol{\xi}|), \quad \text{where} \quad F(|\mathbf{x} - \boldsymbol{\xi}|) \equiv (\pi\sigma)^{-3/2} \exp(-\sigma^{-1}|\mathbf{x} - \boldsymbol{\xi}|^2).$$

5. Discussion. We have developed a hybrid asymptotic-numerical approach to analyze the existence, linear stability, and slow dynamics of quasi-equilibrium N -spot patterns for the singularly perturbed three-dimensional (3-D) Schnakenberg model (1.2) in the limit $\varepsilon \rightarrow 0$. In terms of the original model (1.1), such patterns occur in the large diffusivity regime $D = \mathcal{O}(\varepsilon^{-4})$. Our hybrid asymptotic-numerical framework characterizing the linear stability of quasi-equilibrium spot patterns and slow spot dynamics was implemented numerically for some spot patterns in the unit ball. Our linear stability results and asymptotic predictions for the slow spot dynamics were shown to compare very favorably with results obtained from full numerical simulations of the 3-D Schnakenberg model (1.2) using FlexPDE6 [6].

We now briefly discuss a few open problems that warrant further study. Our implementation of slow spot dynamics was done only for the case where Ω is the unit ball, for which

there is an explicit analytical formula for the Neumann Green's function and its regular part. To leading order in ε , the slow ODE dynamics in (4.18) for a spatially uniform feed A , and in (4.32) for a variable feed $A(\mathbf{x})$, depend on the gradient of this Neumann Green's function. For more complicated domains, it would be interesting to implement the explicit ODE dynamics numerically by using fast multipole methods (cf. [8]) to compute the required Green's function both accurately and rapidly. Such fast multipole methods would be highly advantageous in this setting, since in simulating the ODE dynamics in (4.18) or (4.32) the gradients of the Green's function must be evaluated at each discrete point of the discretization of the ODE dynamics. With this approach it should be tractable to numerically study spot dynamics and, in particular, spot-pinning effects due to either changes in the domain geometry or spatial variations in the variable feed-rate $A(\mathbf{x})$.

For the case where $A > 0$ is constant, a second open problem is to identify stable equilibria of the leading-order ODE dynamics (4.18) that have large basins of attraction for initial conditions. As N increases, the energy landscape of the discrete energy \mathcal{H} in (4.17) will have an increasingly large number of local minima with nearly the same energy (cf. [3] and the references therein). These local minima are all linearly stable equilibrium points of (4.18). A natural question is to study, as N increases, whether most initial conditions for (4.18) tend to the global minimum point of \mathcal{H} . Our computations of (4.18) for random configurations of spots have suggested that this property holds: $N = 2, \dots, 20$. For the unit ball, the global minimum of \mathcal{H} for $N = 2, \dots, 20$ was computed using numerical optimization software in [3], but it becomes computationally much more challenging to compute it for larger N . Therefore, in what sense can the ODE system (4.18) be used as a regularization for computing the global minimum point of \mathcal{H} ? From a numerical analysis viewpoint, a related ODE regularization was used in [16] to compute a minimum energy configuration for 2-D Coulomb particles on the surface of a ball. We remark that the identification of the global minimum point of \mathcal{H} also arises in other contexts. In particular, it corresponds to the spatial configuration of the centers of small traps that minimize the average mean first passage time for a Brownian walker in a 3-D domain [3] that has a uniformly distributed starting point in the domain.

A related open question is to identify steady-state spatial configurations of (4.18) for which $\mathbf{e} = (1, \dots, 1)^T$ is an eigenvector of the Neumann Green's matrix \mathcal{G} . When this condition holds, we determined an improved approximation for the competition stability threshold in Main Result 3.1 that involves the minimum eigenvalue of \mathcal{G} in the subspace orthogonal to \mathbf{e} . In this case, asymmetric spot equilibrium solution branches all bifurcate from the symmetric solution branch at a common point. In contrast, if \mathbf{e} is not an eigenvector of \mathcal{G} at the steady-state of (4.18), we can expect an intricate imperfection-sensitive bifurcation structure near the competition instability threshold. Although we studied this delicate behavior analytically near the competition instability threshold for the case $N = 2$ in (2.44) of section 2.1, it is an open issue to locally examine this imperfection sensitivity analytically for larger N .

Finally, we remark that it should be possible to develop a similar hybrid asymptotic-numerical approach to study localized quasi-equilibrium spot patterns in a 3-D setting for other well-known singularly perturbed reaction-diffusion systems, such as the Gierer–Meinhardt, Gray–Scott, and Brusselator models.

REFERENCES

- [1] I. BARRASS, E. J. CRAMPIN, AND P. K. MAINI, *Mode transitions in a model reaction–diffusion system driven by domain growth and noise*, Bull. Math. Biol., 68 (2006), pp. 981–995.
- [2] W. CHEN AND M. J. WARD, *The stability and dynamics of localized spot patterns in the two-dimensional Gray–Scott model*, SIAM J. Appl. Dyn. Syst., 10 (2011), pp. 582–666, <https://doi.org/10.1137/09077357X>.
- [3] A. CHEVIAKOV AND M. J. WARD, *Optimizing the principal eigenvalue of the Laplacian in a sphere with interior traps*, Math. Comput. Model., 53 (2011), pp. 1394–1409.
- [4] E. J. CRAMPIN, E. A. GAFFNEY, AND P. K. MAINI, *Reaction and diffusion on growing domains: Scenarios for robust pattern formation*, Bull. Math. Biol., 61 (1999), pp. 1093–1120.
- [5] A. DHOOGHE, W. GOVAERTS, AND Y. A. KUZNETSOV, *MATCONT: A MATLAB package for numerical bifurcation analysis of ODEs*, ACM Trans. Math. Software (TOMS), 29 (2003), pp. 141–164.
- [6] *FlexPDE 6*, PDE Solutions Inc., Spokane, WA, 2016, <http://www.pdesolutions.com>.
- [7] E. A. GAFFNEY AND N. A. M. MONK, *Gene expression time delays and Turing pattern formation systems*, Bull. Math. Biol., 68 (2006), pp. 99–130.
- [8] L. GREENGARD AND V. ROKHLIN, *A new version of the fast multipole method for the Laplace equation in three dimensions*, Acta Numer., 6 (1997), pp. 229–269.
- [9] D. IRON AND M. J. WARD, *A metastable spike solution for a nonlocal reaction-diffusion model*, SIAM J. Appl. Math., 60 (2000), pp. 778–802, <https://doi.org/10.1137/S0036139998338340>.
- [10] D. IRON, J. WEI, AND M. WINTER, *Stability analysis of Turing patterns generated by the Schnakenberg model*, J. Math. Biol., 49 (2004), pp. 358–390.
- [11] T. KOLOKOLNIKOV, M. J. WARD, AND J. WEI, *The existence and stability of spike equilibria in the one-dimensional Gray–Scott model: The pulse-splitting regime*, Phys. D, 202 (2005), pp. 258–293.
- [12] T. KOLOKOLNIKOV, M. J. WARD, AND J. WEI, *Spot self-replication and dynamics for the Schnakenberg model in a two-dimensional domain*, J. Nonlinear Sci., 19 (2009), pp. 1–56.
- [13] Y. NISHIURA, *Far-from Equilibrium Dynamics*, Transl. Math. Monogr. 209, AMS, Providence, RI, 2002.
- [14] I. ROZADA, S. J. RUUTH, AND M. J. WARD, *The stability of localized spot patterns for the Brusselator on the sphere*, SIAM J. Appl. Dyn. Syst., 13 (2014), pp. 564–627, <https://doi.org/10.1137/130934696>.
- [15] J. SCHNAKENBERG, *Simple chemical reaction systems with limit cycle behaviour*, J. Theor. Biol., 81 (1979), pp. 389–400.
- [16] W. STORTELDER, J. DE SWART, AND J. PINTÉR, *Finding elliptic Fekete point sets: Two numerical solution approaches*, J. Comput. Appl. Math., 130 (1998), pp. 205–216.
- [17] W. SUN, M. J. WARD, AND R. RUSSELL, *The slow dynamics of two-spike solutions for the Gray–Scott and Gierer–Meinhardt systems: Competition and oscillatory instabilities*, SIAM J. Appl. Dyn. Syst., 4 (2005), pp. 904–953, <https://doi.org/10.1137/040620990>.
- [18] P. TRINH AND M. J. WARD, *The dynamics of localized spot patterns for reaction-diffusion systems on the sphere*, Nonlinearity, 29 (2016), pp. 766–806.
- [19] V. K. VANAG AND I. R. EPSTEIN, *Localized patterns in reaction-diffusion systems*, Chaos, 17 (2007), 037110.
- [20] M. J. WARD AND J. WEI, *The existence and stability of asymmetric spike patterns for the Schnakenberg model*, Stud. Appl. Math., 109 (2002), pp. 229–264.
- [21] M. J. WARD AND J. WEI, *Hopf bifurcation of spike solutions for the shadow Gierer–Meinhardt model*, Eur. J. Appl. Math., 14 (2003), pp. 677–711.
- [22] J. WEI AND M. WINTER, *Spikes for the two-dimensional Gierer–Meinhardt system: The weak coupling case*, J. Nonlinear Sci., 11 (2001), pp. 415–458.
- [23] J. WEI AND M. WINTER, *Asymmetric spotty patterns for the Gray–Scott model in \mathbb{R}^2* , Stud. Appl. Math., 110 (2003), pp. 63–102.
- [24] J. WEI AND M. WINTER, *Existence and stability of multiple spot solutions for the Gray–Scott model in \mathbb{R}^2* , Phys. D, 176 (2003), pp. 147–180.
- [25] J. WEI AND M. WINTER, *Stationary multiple spots for reaction-diffusion systems*, J. Math. Biol., 57 (2008), pp. 53–89.
- [26] S. XIE AND T. KOLOKOLNIKOV, *Moving and jumping spot in a two dimensional reaction diffusion model*, Nonlinearity, submitted.